


## Article

# A Simplified Inverse Analysis Procedure for the Stress-Crack Opening Relationship of Fiber-Reinforced Concrete

Pedro Paulo Martins de Carvalho <sup>1,\*</sup> and Rodrigo de Melo Lameiras <sup>2</sup> <sup>1</sup> Center of Exact Sciences and Technologies, Federal University of Western Bahia, Barreiras 47810-047, BA, Brazil<sup>2</sup> Postgraduate Program in Structures and Civil Construction, University of Brasilia, Brasilia 70910-900, DF, Brazil

\* Correspondence: pedro.carvalho@ufob.edu.br

**Abstract:** The direct tensile test (DTT) is the most recommended test to determine the tensile behavior of fiber-reinforced concrete (FRC). However, this test is challenging to perform. Several studies have investigated inverse analysis to determine this behavior through simplified tests, such as the bending test. This study deals with developing a new approach to perform an inverse analysis for the three-point bending test (3PBT) involving FRC. A new proposed methodology concerns carrying out the inverse analysis procedure by parts. Initially, the parameters that influence the initial part of the stress–crack opening curve are adjusted. Progressively, the other parameters are adjusted considering the increment of the curve section. This procedure provides an implemented algorithm with more efficiency. A new strategy that deals with the establishment of criteria for parameters is proposed. Its results are compared with experimental data from other literature, whose steel fiber-reinforced concrete (SFRC) tested characteristics present different attributes such as fibers, shape, and length. The proposed methodology obtained the stress–crack opening curves in direct tension with reasonable accuracy, indicating that this methodology can be helpful in the characterization of the post-cracking FRC behavior.

**Keywords:** inverse analysis; crack length; stress–crack width; steel fiber-reinforced concrete; three-point bending test; post-cracking behavior



**Citation:** Carvalho, P.P.M.d.; Lameiras, R.d.M. A Simplified Inverse Analysis Procedure for the Stress-Crack Opening Relationship of Fiber-Reinforced Concrete. *Buildings* **2023**, *13*, 1166. <https://doi.org/10.3390/buildings13051166>

Academic Editor: Junjie Zeng

Received: 1 March 2023

Revised: 4 April 2023

Accepted: 7 April 2023

Published: 28 April 2023



**Copyright:** © 2023 by the authors. Licensee MDPI, Basel, Switzerland. This article is an open access article distributed under the terms and conditions of the Creative Commons Attribution (CC BY) license (<https://creativecommons.org/licenses/by/4.0/>).

## 1. Introduction

In the inverse analysis problem, the results provided in a given experiment, for example, are used to determine the input data of the direct problem, or the input data are used to determine the properties of a system [1–3]. Reference [4] uses direct analysis (a procedure that requires the definition of the form of the constitutive relationship, in order to simulate the uniaxial behavior of the material) and inverse analysis, which deals with the interactive solution to determine stress-strain or stress-opening diagrams of cracks based on the adjustment of experimental results through constitutive relations.

An essential type of application of applying inverse analysis consists of obtaining stress ( $\sigma$ )–crack opening displacement (COD) using the experimental response of force-displacement in a test with fiber reinforced concrete (FRC) samples. FRC has several significant mechanical properties, such as fracture toughness, ductility, durability, and crack width control [5–8]. The inverse analysis application is helpful to FRC because the indicated test that obtains information on post-cracking behavior directly (the direct tensile test—DTT) is challenging to perform [9]. Therefore, the inverse analysis procedure starts from the knowledge of concrete and fiber properties and the experimental response of the three-point bending test (3PBT) to estimate the tensile response ( $\sigma$ –COD) (Figure 1). The inverse analysis involves carrying out an interactive procedure to determine values for the parameters that describe the direct tensile behavior, based on the bending response. It is

established that the set of parameters that characterize a material's tensile behavior leads to the slightest error in the bending behavior.

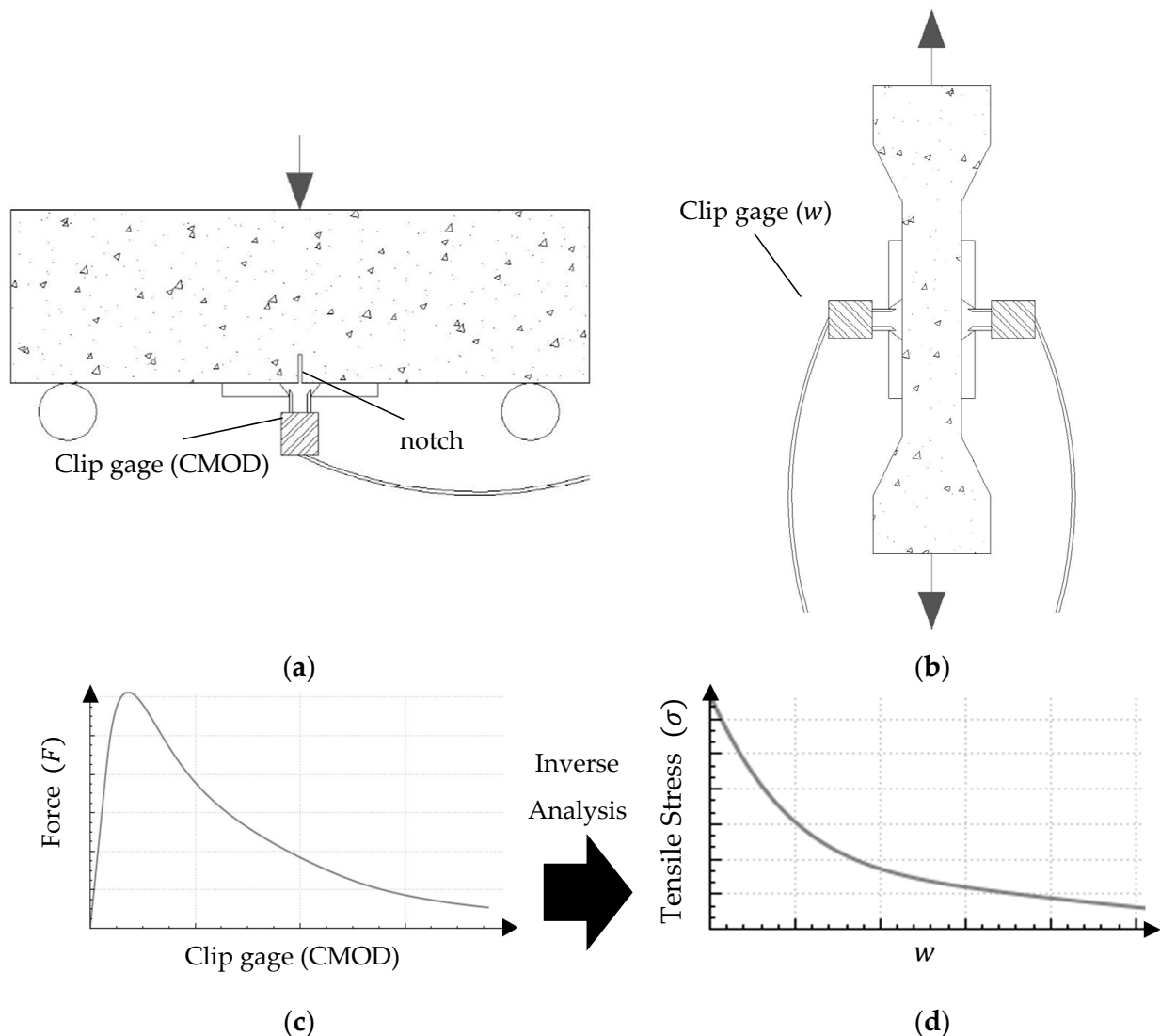


**Figure 1.** Inverse analysis procedure: (a) 3PBT, (b) DTT, (c) Force (F)–Crack Mouth Opening Displacement (CMOD) from 3PBT, (d) Stress ( $\sigma$ )–Crack Opening Displacement (w) curve from inverse analysis (represents the DTT).

A significant milestone in the study of the FRC tensile behavior was the development of the fictitious crack model [10]. In this model, the understanding of the complex behavior of this composite is simplified by considering linear relationships before cracking. In addition, the formation of cracks allows the consideration of a stress transmission bridge across the cracks. A model was developed [11] for the behavior of FRC beams with a 3PBT test based on the force balance in the critical section. The results of this model lead to the conclusion that the bending performance of FRC is strongly influenced by the Force (F)–Crack Mouth Opening Displacement (CMOD) curve. This curve presents an initial section that is approximately linear, and after the initiation of the fracturing process, the post-cracking section occurs [12–16]. From this section, the F–CMOD curve becomes more challenging to estimate, requiring the implementation of complex models.

The inverse analysis procedure for FRC can be performed using two approaches: analytical and numerical. In the numerical approach, input data (geometric boundary conditions and material behavior laws) are obtained through numerical simulations. Therefore,

there is the disadvantage of the high computational cost and the need to apply a numerical model, for example, based on the finite element method (FEM). This approach has already been applied in its conventional form to the SFRC [17–23], for FRC with recycled fiber [24,25], and in specimen situations with different notch depths and sizes [26]. Still using this approach, [27] performed an inverse analysis procedure involving a graphical analysis process. Initially, relationships are established for the defining parameters of post-cracking behavior and boundary conditions. Simulations based on a program involving the FEM are then performed.

The numerical responses obtained for the 3PBT are compared with the experimental response via graphical analysis. The behavior under direct tensile ( $\sigma$ –COD), which leads to the slightest error in the F–CMOD curve on bending, is the result of the inverse analysis. Despite successfully carry out the inverse analysis, the numerical approach has some limitations, among which the following can be mentioned:

- The need to use specific computational programs for structural analysis;
- The high computational cost;
- The significant time spent performing the inverse analysis.

In this context, the search for new ways of implementing this procedure is justified, especially in a simplified way.

The analytical approach is based on establishing constitutive laws of the post-cracking behavior of FRC. Compatibilizations are performed between the deformations considering the behavior studied before cracking and post-cracking. Equations are usually applied that define the behavior of the composite based on research or normative codes. Within this approach, models have been employed for the behavior of FRC beams with 3PBT based on the force balance in the critical section [11], including the Monte Carlo method [28]; there is another proposal that divides the analysis into stages involving initial estimation of parameters and subsequent adjustment of curves [29]. Some studies emphasized analytical approaches involving plastic hinges [30,31], including approaches concerning parameter optimization by probabilistic means [32] and the global fitting strategy.

The inverse analysis procedure that several literature results have studied still has limitations [5,21,22,25,26,29,32–35]. One is the high computational cost for implementing numerical or analytical models. Suppose simplifications such as those proposed in this study need to be established. In that case, the procedure may result in numerous combinations of parameters to be calculated at all levels studied. Errors are usually also calculated considering the full Force–CMOD curve and require high computational cost for forming the  $\sigma$ – $w$  (tensile-crack opening displacement) answer.

This study contributes to this gap. A new simplified proposal for the inverse analysis procedure was developed. In the usual inverse analysis procedure, the input data are selected randomly or without a choice criterion, which leads to a high computational cost. In this study, the input parameters are determined according to the fiber length, which is considered a factor of relevant influence on the FRC tensile behavior [9,36,37], including for the inverse analysis procedure. Furthermore, the inverse analysis procedure is performed progressively, first determining the parameters that determine the initial part of the response  $\sigma$ – $w$ . Only afterward the other parameters are adjusted. It is considered that the initial parameters of the response  $\sigma$ – $w$  influence only part of the Force–CMOD curve, as graphically observed by [27]. The methodology presented in this study made the computational process more efficient since it considers that the initial parameters of the  $\sigma$ – $w$  influence only a portion of the Force–CMOD curve. Thus, each set of response curve parameters  $\sigma$ – $w$  is adjusted considering the Force–CMOD error up to a given CMOD. The usual inverse analysis procedure performed by other literature [29,31] is also part of estimating the initial parameters. Therefore, it is proposed to determine the parameters by parts, first adjusting the parameters of the initial section of the  $\sigma$ – $w$  curve, then calculating the error of only part of the curve. The process significantly reduces the number of program steps.

Despite [27] performing a study for initial parameter estimates, the author's study has the disadvantage of using a proposal based on the finite element method (FEM). In [31], research was carried out with an analytical methodology for the inverse analysis; however, no strategic estimation of the initial parameters was established. Therefore, this study produces an essential contribution by combining the advantages of these two studies by employing an analytical methodology with a strategic estimation of initial parameters, which tends to reduce the computational cost of inverse analysis significantly.

## 2. Three-Point Bending Test (3PBT)

The post-cracking tensile behavior of FRC is the most fundamental property of this composite. To properly determine this behavior, technical standards [38–40] usually recommend three-point bending (3PBT) tests and estimate the tensile behavior through useful simplifications for projects.

The 3PBT test is widely used due to its simplicity of execution (also present in the other indirect tensile tests) about the direct tensile test. The main disadvantage, however, is the need to employ a relatively behavior deduction or perform an inverse analysis [41]. The 3PBT is a good test for FRC classification [6].

The performance of the 3PBT test consists of applying a load to a prismatic specimen supported by a central notch, which reduces the dispersion of the test results by inducing notch cracking itself (Figure 1a). A transducer (such as a clip gage, as shown in Figure 1a) is usually used at the base of the sample to monitor the relative displacement between two points close to the notch. The measured displacement is called CMOD (Crack Mouth Opening Displacement). The load is monitored during the test. At the end of the test, a Force–CMOD curve is obtained that characterizes the material tested.

The limit of proportionality ( $f_{fct,L}$ ) and the flexural tensile strength ( $f_{Rj}$ ), corresponding with CMOD<sub>j</sub> with  $j = 1, 2, 3, 4$ , is obtained during the test. The  $f_{Rj}$  are used to identify the constitutive law [40]:

$$f_{R,j} = \frac{3F_j l}{2bh_{sp}^2} \quad (1)$$

where  $F_j$  is the load corresponding with CMOD = CMOD<sub>j</sub>,  $l$  is the span length [mm],  $b$  is the width of the specimen [mm], and  $h_{sp}$  is the distance between the notch tip and the top of the specimen [mm], 125 mm.

## 3. Analytical Model for Determination of (F–CMOD)<sub>anal</sub> Diagrams

Several models have already analytically determined F–CMOD behavior. [5,17–21]. In this study, the model described by [31] was used. Therefore, this section is limited to describing the model proposed by this author.

The model proposed by [31] starts from the consideration of a bending beam with a width section  $b$  and height  $H$  with a notch that makes it present effective height  $h$ , acting for a moment  $M$  in the sample under the imposition of a rotation  $\theta$  (Figure 2).

The sample section is divided into layers to which constitutive laws of compressive and tensile behavior. The value of  $L_s$  is the beam's length and  $L_h$  is the length of the non-linear hinge. The extension due to a rotation  $\theta_k$  was calculated in an interaction  $k$  per unit of  $L_h$  for the  $i$ -th layer ( $D_i^k$ ) with Equation (2) (Figure 2b,c):

$$D_i^k = \theta_k \times (d_i - d_{na}) \quad (2)$$

where  $d_i$  and  $d_{na}$  corresponds to layer depth  $i$  and the neutral line, respectively.

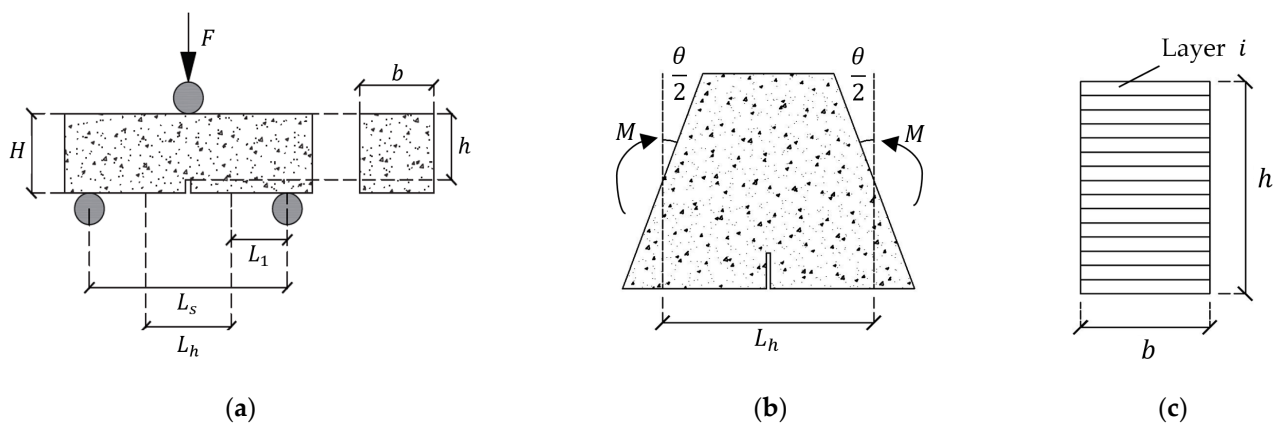


**Figure 2.** Representative scheme of the beam under the 3PBT test, highlighting: (a) notch and length of the plastic hinge ( $L_h$ ), (b) plastic hinge model, and (c) layering of the cross-section. Adapted from [31].

Knowing the compressive behavior for the inverse analysis procedure is essential when the analyzed sample is under bending stress. In the present study, the FRC compressive behavior is given by a well-studied constitutive model. The compression force  $F_{cc}^k$  and the tensile force  $F_{ct,i}^k$  are determined by constitutive relations as a function of  $\epsilon_{ef,i}^k$ . The value of  $\epsilon_{ef,i}^k$  is obtained by dividing  $D_i^k$  by  $L_h$ . It is more significant than the strain ( $\epsilon_{ct,p}$ ) corresponding to tensile strength  $f_{ct}$ , the section is considered cracked; therefore, the isolated constitutive equations do not represent this behavior satisfactorily. In these cases, we have:

$$F_{ct,i}^k = \sigma_{ct}(w_i^k)bt \quad (3)$$

where  $\sigma_{ct}$  is the tensile stress,  $w_i^k$  is the crack opening for the layer  $i$  for the rotation increment interaction,  $k$ , and  $t$  is the thickness of each layer. The moment-rotation is calculated considering the balance of moments of the cross-section. The moment at the edge of the length  $L_h$  (Figure 2a) follows the relationship of Equation (4), from which we can calculate the characteristic strength ( $F_k$ ). For the compressive behavior, we disregard the pre-peak influence and use the model of [42] modified by [43] for SFRC with fibers whose ends are hooked. A multilinear model based on [44] can be used for the tensile behavior. The bending moment,  $M_k$ , is:

$$M_k = 0.25F_k(L_s - 0.5L_h) \quad (4)$$

The deflection  $\delta_k$  is calculated based on the virtual work method, considering the sum between a plastic and an elastic portion, according to Equation (5).  $I_1$  and  $I_2$  correspond to the notched and unnotched sections' moments of inertia, respectively.

$$\delta_k = \frac{F \left( \frac{L_s - L_h}{2} \right)^3}{6E_c I_2} \left[ \left( \frac{L_s}{L_s - L_h} \right)^3 + \left( \frac{I_1}{I_2} - 1 \right) \right] + \frac{L_s \theta}{4} \quad (5)$$

where  $E_c$  is the elastic modulus determined according to [40].

There is no consensus established in the literature for the value of  $L_h$ . The typical values are  $h$ ,  $h/2$ , and  $2h$  [31,39,45–49]. In the proposed study, the value  $h/2$  was adopted.

The flowchart in Figure 3 illustrates the procedure presented in this section.

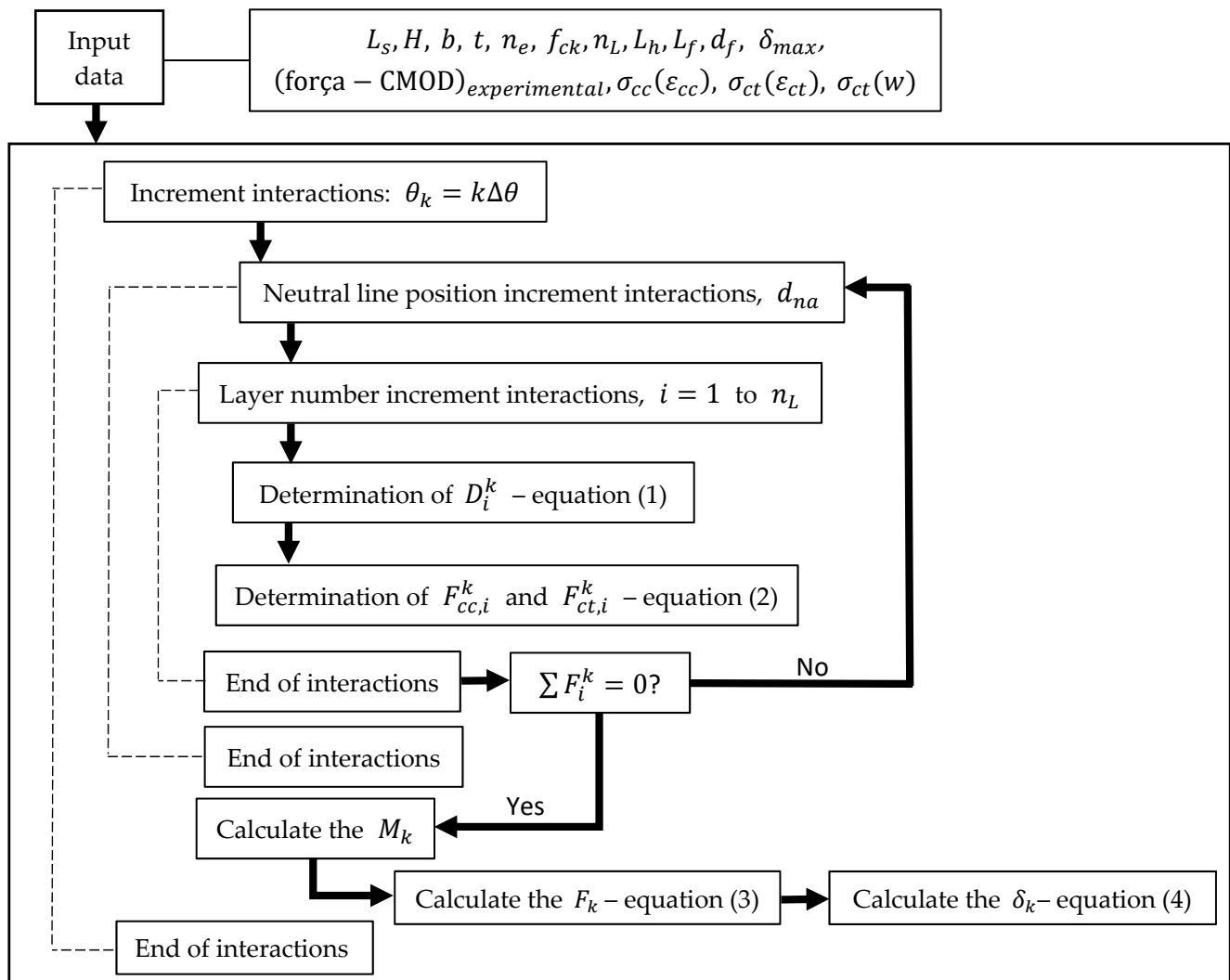


**Figure 3.** Illustration of the representative model of the post-cracking behavior of FRC to determine the response  $F - \delta$ . Adapted from [31]. Here,  $L_f$  and  $d_f$  are length and diameter of the fibers, respectively,  $n_L$  is the number of layers;  $n_e = H - h$ ,  $\sigma_{cc}(\epsilon_{cc})$  is the compressive stress [43], and  $\sigma_{ct}(\epsilon_{ct})$  is the tensile stress from bilinear stress-strain [40].

#### 4. The Inverse Analysis Procedure

##### 4.1. The Concept of Inverse Analysis

The inverse analysis procedure aims to find the stresses  $\sigma_1, \sigma_2$ , and  $\sigma_3$  corresponding to the crack openings  $w_1, w_2$  and  $w_3$ . These parameters represent points on the  $\sigma$ - $w$  diagram obtained as a result of applying the inverse analysis procedure that define the direct tensile quadrilinear post-cracking behavior of FRC. For analysis, initially, it is necessary to estimate these values for the algorithm. A proposal to estimate these values is presented in Section 4.2.1.

A flowchart illustrating the inverse analysis procedure and work steps are shown in Figure 4. The procedure is performed progressively to determine  $\sigma$ - $w$  from a multilinear model, whereas this study offers the approach for a quadrilinear response.

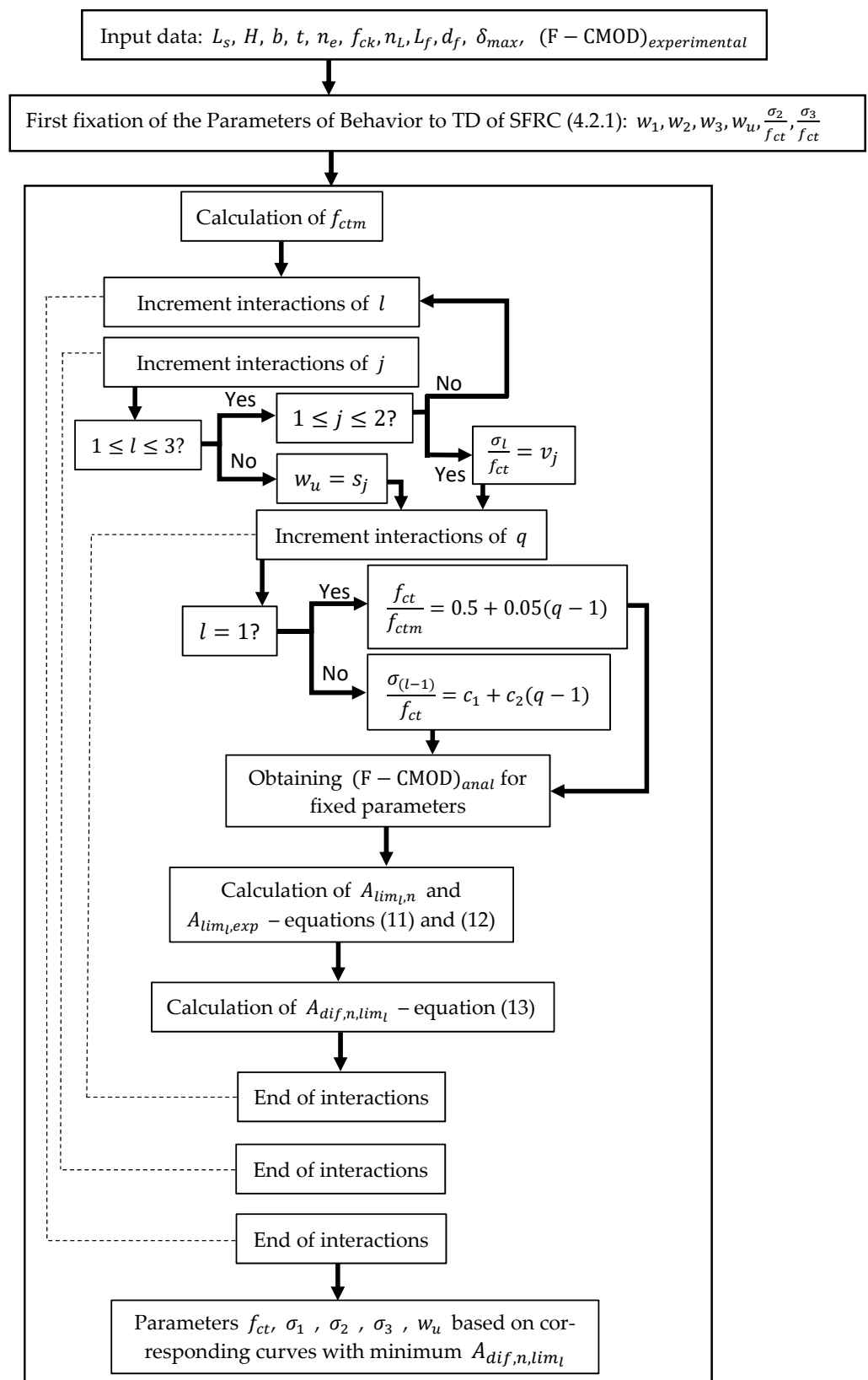


**Figure 4.** Algorithm general for performing the inverse analysis procedure with  $f_{ctm}$  obtained according to [40] and  $(F - CMOD)_{anal}$  obtained according to [31] model.

For executing the inverse analysis procedure, the program starts with the input parameters, which are described below:



- Parameters of the tested sample: span ( $L$ ), height ( $H$ ), width ( $b$ ), and notch depth ( $n_e = H - h$ ), according to Figure 4;
- Concrete parameters: compressive strength ( $f_{ck}$ ) and tensile strength ( $f_{ct}$ ) of FRC;  $f_{ctm}$  is the average tensile strength obtained according to [40];
- Fiber parameters: length ( $L_f$ ) and diameter ( $d_f$ );
- In order to determine the error, the experimental results of the F-CMOD curve,  $(F-CMOD)_{exp}$  curve, were obtained through experimental results of the 3PBT must be input data, as well as the maximum deflection ( $\delta_{max}$ ).

$l$  is the index varying from 1 to 4 for increment interactions of the steps in which each variable are fixed;  $j$  is the index varying from 1 to 3 for increment interactions for determination of  $s_j$ , which corresponds to the values set for  $w_u$ ;  $q$  is the index varying from 1 to 13 for increment interactions of the steps in which we determined  $f_{ct}$ ,  $\sigma_1$ ,  $\sigma_2$ , and  $\sigma_3$ ;  $v_j$  corresponds to the values fixed for the relations  $\sigma_1/f_{ct}$ ;  $A_{lim_1,n,i}$  is the area of the  $i$ -th segment of the  $n$ -th analytical curve;  $A_{lim_1,exp,i}$  is the area of the  $i$ -th section of the experimental curve; and  $A_{dif,n,lim_1}$  corresponds to the differences between each of the  $n$  areas of the analytical response and the experimental response.

The parameters for tensile are estimated, and the bending response is analyzed. It is considered that the set of parameters that characterize the material's tensile behavior leads to the slightest error in the bending behavior. The diagrams  $(F-CMOD)_{anal}$  are obtained analytically through the method based on [31], according to the flowchart shown in Figure 3. The inverse analysis process is applied to determine the stress-opening of cracks ( $\sigma$ - $w$ ).

#### 4.2. Parameters of SFRC Direct Tensile Behavior

This study proposes carrying out an inverse analysis through a strategy that involves selecting appropriate initial parameters among those that most influence the post-cracking behavior of FRC to employ an analytical model and then generate the F-CMOD curve. This way, this procedure obtains a more rational method. In the analytical procedure, fracture mechanics parameters of the FRC tensile behavior (crack opening ( $w_i$ ) and corresponding stress  $\sigma_i = A_i f_{ct}$ ) are predefined (Figure 5). Then, algorithms perform a series of iterations to find parameters that solve the inverse problem and determine the answer  $\sigma$ - $w$ , leading to the slightest error in the answer of F-CMOD. To reduce the computational effort, a strategy based on the previous experience of [27] was employed. First, some initial tensile parameters ( $\sigma$ - $w$ ) are strategically estimated.

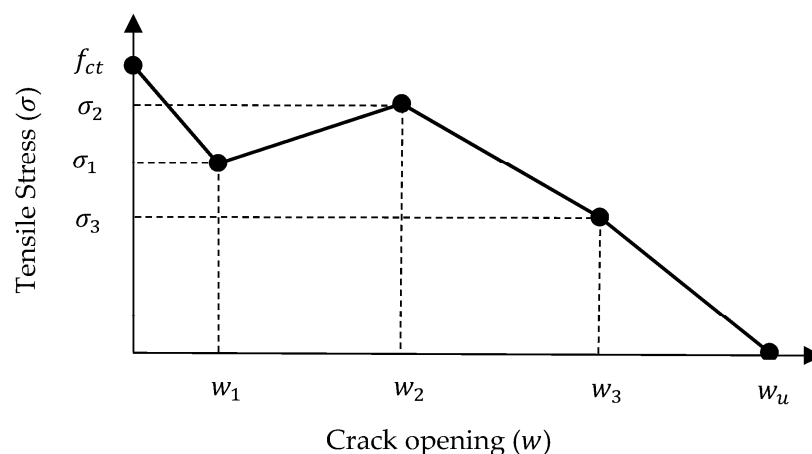


**Figure 5.** Illustration of the representative quadrilinear model of the FRC post-cracking behavior.

##### 4.2.1. Initial Parameters Determination

In this step, the initial parameters of the algorithm are established based on the experience of [27]. The author used fixed values for initial parameters of  $w$ :  $w_1 = 0.2$  mm,  $w_2 = 1.0$  mm, and  $w_3 = 2.5$  mm. However, the need to change these parameters is



considered reasonable, mainly due to the variation in fiber length. Furthermore, this study evaluated the possibility of working with concrete with different characteristics. Therefore, equations were determined to define the three initial parameters of  $w$ . Finally, the  $w_1$  parameter was calculated with Equation (6):

$$w_1 = \frac{L_f}{175} \quad (6)$$

In early-stage interactions, the ultimate crack opening is initially estimated as  $w_u = L_f/8$ , considering a fiber efficacy factor of 0.25 [17,47]. Therefore, for uniformity of the quadrilinear model, we have the Equations (7) and (8):

$$w_2 = \frac{\frac{L_f}{8} - w_1}{3} \quad (7)$$

$$w_3 = 2 \frac{\frac{L_f}{8} - w_1}{3} \quad (8)$$

The values  $w_1$ ,  $w_2$ , and  $w_3$  are fixed for the entire procedure. At this initial stage and during the process of determining  $f_{ct}$ , the following values are fixed:  $\sigma_2/f_{ct} = 1.0$  and  $\sigma_3/f_{ct} = 0.5$ .

#### 4.2.2. Determination of $f_{ct}$

In the present step, the algorithm determines the tensile strength value ( $f_{ct}$ ). Then, the value of  $f_{ctm}$  is calculated according to the recommendations of [40]. The analytical model is implemented for the relationship of  $\sigma_1/f_{ct} = v_1$  and  $\sigma_1/f_{ct} = v_2$ . The ratio  $\sigma_1/f_{ct}$  is considered the second variable in this step, and  $f_{ct}/f_{ctm}$  is the primary variable. The second variable values ( $v_1$  and  $v_2$ ) were taken at 20% above and below the unit value for this and the other steps of this method. Therefore, we have:  $v_1 = 0.8$  and  $v_2 = 1.2$ .

The relation  $f_{ct}/f_{ctm}$  considered were corresponding to the interval [0.5–1.1], varying at a given step. The lower part, or equal to 0.9 of this range (from 0.5 to 0.9), was chosen because, in notched specimens, the maximum stress may be much lower than the cracking stress. After all, the stresses are concentrated in the notch [27]. Comparing the results of this methodology with other research [24,29,31], it was verified that the range from 0.9 to 1.1 was also consistent for certain types of concrete. The variation step (0.05) was chosen as half of the stage adopted for the following steps because the curves obtained due to executing this step showed greater sensitivity for the variable  $f_{ct}/f_{ctm}$  and because this is the primary variable in this step. Therefore, we obtain:

$$\frac{f_{ct}}{f_{ctm}} = 0.5 + 0.05(q - 1) \quad (9)$$

where  $q$  ranges from 1 to 13, according to the flowchart in Figure 4.

The program then verifies, among the curves obtained, the one that best fits the first part of the diagram, comparing  $(F - CMOD)_{exp}$  with  $(F - CMOD)_{anal}$ , according to Section 4.2.6. An illustration of this procedure can be seen in Figure 6. In this case, the first branch is defined between 0 and  $w_1$  since it is significantly influenced by the relationship  $f_{ct}/f_{ctm}$ . The solid lines represent the answers  $(F - CMOD)_{anal}$  and the dashed line represents  $(F - CMOD)_{exp}$ . Subsequently, the algorithm calculates the area under each curve  $(F - CMOD)_{anal}$  in this stretch and compares it with the estimated area under curve  $(F - CMOD)_{exp}$ , as detailed in Section 4.2.6.

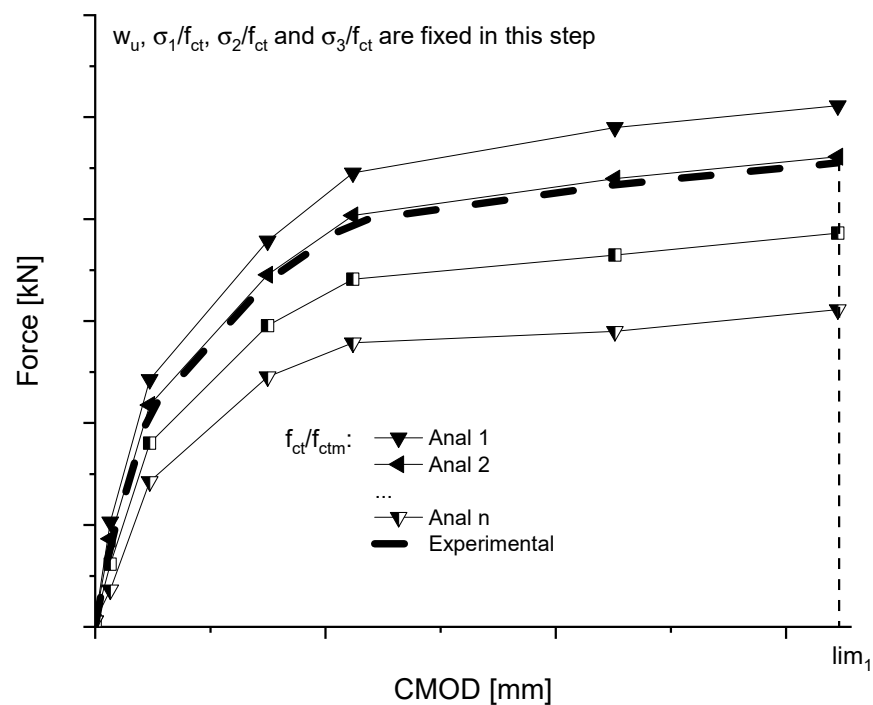


**Figure 6.** Area calculation branch for CMOD between 0 and  $lim_1$ .

#### 4.2.3. Determination of $\sigma_1/f_{ct}$

In addition to the parameters initially defined, the relation  $f_{ct}/f_{ctm}$ , once  $f_{ct}$  and  $f_{ctm}$ , is already determined in the previous step. In this stage, interactively, the interval values [0.4–1.6] to  $\sigma_1/f_{ct}$  with a step doubled concerning the previous step (0.1). Consequently:

$$\frac{\sigma_{(l-1)}}{f_{ct}} = c_1 + c_2(q - 1) \quad (10)$$

where  $q$  ranges from 1 to 13, according to the flowchart of Figure 4, in which  $c_1 = 0.4$  and  $c_2 = 0.1$  in this step. The ratio  $\sigma_1/f_{ct}$  corresponds to the primary variable, and  $\sigma_2/f_{ct}$  was the secondary variable; that is, it presented the values  $v_1$  and  $v_2$ , as described in Section 4.2.2. With this procedure, the value of  $\sigma_1/f_{ct}$  that best fits the curves obtained  $((F - CMOD)_{exp}$  vs.  $(F - CMOD)_{anal}$ ), so that the error between both is calculated up to certain limits, as described in Section 4.2.6. This procedure is generally illustrated in Figure 7. In this issue, the selected section is significantly influenced by the relation  $\sigma_1/f_{ct}$ . The solid lines represent the answers  $(F - CMOD)_{anal}$ , and the dashed line represents  $(F - CMOD)_{exp}$ . The algorithm then calculates the area under each of the  $(F - CMOD)_{exp}$  curves in this stretch and compares it with the calculated area under the  $(F - CMOD)_{exp}$  curves, as detailed in Section 4.2.6.

#### 4.2.4. Determination of $\sigma_2/f_{ct}$

A procedure similar to the previous step is carried out to determine  $\sigma_2/f_{ct}$ . Although  $\sigma_2/f_{ct}$  becomes the primary variable and  $\sigma_3/f_{ct}$  the secondary, it presented the values  $v_1$  and  $v_2$ , as expressed in Section 4.2.2. The parameter  $\sigma_1/f_{ct}$  is fixed and corresponds to that obtained from the previous step. Furthermore, the parameters  $f_{ct}/f_{ctm}$  (according to the result of Section 4.2.2) and  $w_u = L_f/8$  are fixed. Besides, the same values are established for  $c_1$  and  $c_2$  from the previous step and Equation (10) can be applied to obtain the value of  $\sigma_2/f_{ct}$ .

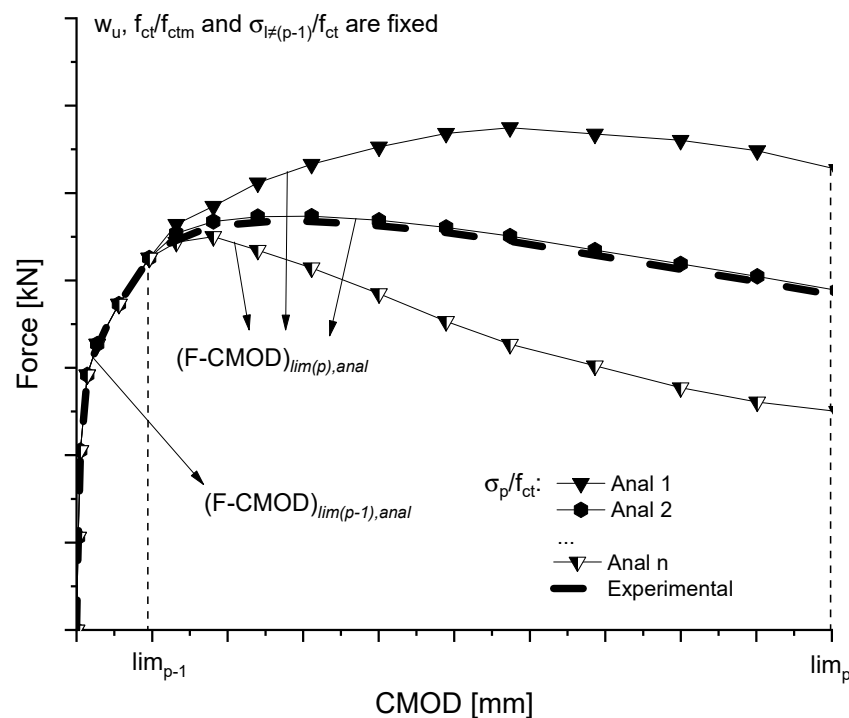


**Figure 7.** Area calculation branches for CMOD between  $lim_{p-1}$  and  $lim_p$ .

#### 4.2.5. Determination of $\sigma_3/f_{ct}$

The procedure is repeated similarly for calculating  $\sigma_3/f_{ct}$ ; this becomes the primary variable and  $w_u$  the secondary variable.  $w_u$  will display the values  $s_1 = L_f/10$ ,  $s_2 = L_f/4$ , and  $s_3 = L_f/8$ . The  $f_{ct}/f_{ctm}$ ,  $\sigma_1/f_{ct}$ , and  $\sigma_2/f_{ct}$  parameters remain the same as those found in Section 4.2.2, Section 4.2.3, and Section 4.2.4, respectively. It was found that  $c_1 = 0.3$  and  $c_2 = 0.1$  are the values that showed greater compatibility between the analytical and experimental responses at this stage. Thus,  $\sigma_3/f_{ct}$  is calculated using Equation (10).

#### 4.2.6. Choice of the Best Fit Curve

A routine was developed to calculate the area under curve of the  $F - CMOD$  diagram to select the curve that best fits the previous steps. For this, the diagram is divided into  $n$  branches. In this step, it was considered that a considerable number of sections can increase the computational effort and a small number can lead to inaccurate results. Therefore, it was decided to increase the refinement concerning the number of stretches only in the region close to the peak.

The choice of CMOD limits to calculate the areas that fit each of the parameters is a significant choice assembled in the procedure proposed in this study. It is observed that these parameters would influence the  $F - CMOD$  curve more until the limits of CMOD are reached in [27]. Thus, the limits established by the author were used. Considering the applied quadrilinear model, these limits will be  $lim_1 = L_f/175$ ,  $lim_2 = L_f/70$ ,  $lim_3 = L_f/17.5$ , and  $lim_4 = L_f/10$ .

An illustration of the area calculation for this procedure is shown in Figures 6 and 7. For the first step (described in Section 4.2.2 of this article), the response areas  $(F - CMOD)_{anal}$  (represented by the continuous lines: Anal 1, Anal 2, ... Anal n) and  $(F - CMOD)_{exp}$  (represented by the thicker dashed line) are calculated for CMOD between 0 and  $lim_1$ , according to Equation (9).

The sections areas of the diagram for each of the  $n$  curves, corresponding to analytical solutions and experimental response ( $exp$ ) are calculated using Equation (11):

$$A_{lim_1, (n \text{ ou } exp), i} = \frac{|F_{i+1} + F_i| \times |CMOD_{i+1} - CMOD_i|}{2} \quad (11)$$

To obtain the analytical and experimental curve areas, the sum presented in Equations (12) and (13) are performed. The areas of the  $n$  analytical curves and the experimental curve contained between 0 and  $lim_1$ :

$$A_{lim_1,n} = \sum_{i=1}^m A_{lim_1,n,i} \quad (12)$$

$$A_{lim_1,exp} = \sum_{i=1}^m A_{lim_1,exp,i} \quad (13)$$

where  $m$  is the number of sections,  $A_{lim_1,n,i}$  is the area of the  $i$ -th section of the  $n$ -th analytical curve, and  $A_{lim_1,exp,i}$  is the area of the  $i$ -th experimental curve section. The procedure is applied for the  $(F - CMOD)_{lim_1,anal}$  and  $(F - CMOD)_{lim_1,exp}$  response.

The following expression gives the differences between the  $n$  areas of the analytical and experimental response:

$$A_{dif,n,lim_1} = |A_{lim_1,n} - A_{lim_1,exp}| \quad (14)$$

Among the  $n$  curves, the one with the lowest value of  $A_{dif,n}$  corresponds to the analytical response  $(F - CMOD)_{lim_1,anal}$  in the region between 0 and  $lim_1$ .

The same procedure is performed for the other sections of the diagram: between  $lim_1$  and  $lim_2$ , between  $lim_2$  and  $lim_3$ , and between  $lim_3$  and  $lim_4$ , i.e., between  $lim_{p-1}$  and  $lim_p$ . An illustration of the procedure is shown in Figure 7.

As described in Section 4.2, for each determination step of an individual parameter ( $f_{ct}$ ,  $\sigma_1$ ,  $\sigma_2$ ,  $\sigma_3$ ,  $w_u$ ), two (or three, in the case of  $w_u$ ) sets of curves are obtained, one for each secondary parameter. Likewise, for any of these sets, there will be an  $A_{dif,n,lim_p}$  corresponding to the secondary parameters. Among these, the algorithm selects the one that presents the slightest difference between the obtained areas of the analytical and experimental response.

At the end of this process, a  $(F - CMOD)_{anal}$  curve is obtained. This curve approximates the  $(F - CMOD)_{exp}$  response obtained through the 3PBT test, as shown in Figure 8. For the respective  $(F - CMOD)_{anal}$  found, the curve representing the tensile behavior  $(\sigma - w)_{anal}$  is obtained.

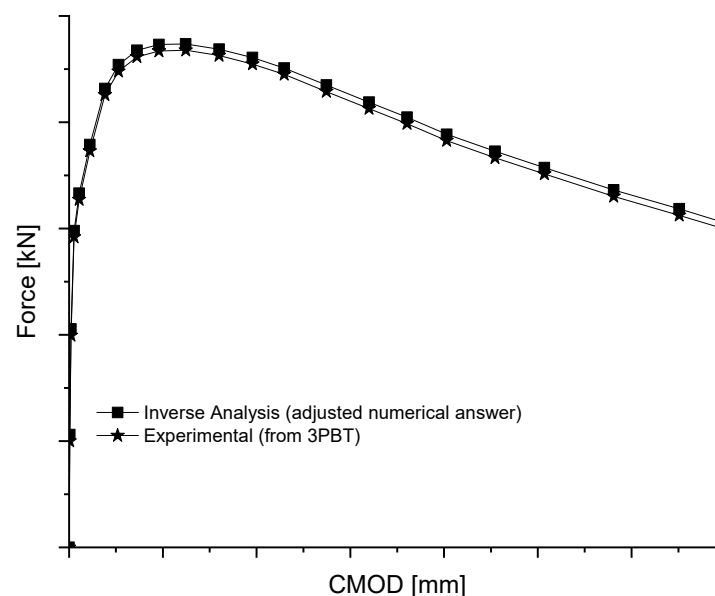


Figure 8. Answer  $(F - CMOD)_{anal}$  vs.  $(F - CMOD)_{exp}$ .

#### 4.2.7. Validation of the Inverse Analysis Procedure

The methodology presented in the previous steps establishes the  $(\sigma - w)_{anal}$  diagram. Then,  $(\sigma - w)_{anal}$  and  $(F - CMOD)_{anal}$  results from inverse analysis performed with experimental validation of four types of FRC from different studies were selected for its validation. Three of the concretes used in the literature were reinforced with conventional steel fibers with hook-shaped ends (HE) and one with recycled steel fibers with variable end shapes and dimensions. In addition, the concretes presented different types: self-compacting (SFRSCC) and conventional (SFRC), with different  $f_{ck}$  values and fiber form factors. These characteristics are described in Table 1.

**Table 1.** Characteristics of the analyzed fibers and concretes.

Author	Denomination	$f_{ck}$ [MPa]	$f_{ct}$ [MPa]	Fiber Length/ Diameter Ratio ( $L_f/d_f$ ) [mm/mm]	Fiber Kind	Concrete Kind
[27]	SFRSCC B	55	2.23	35/0.55	Steel, HE	SFRSCC
[31]	C45-f90	45	2.4	35/0.55	Steel, HE	SFRSCC
[24]	RSFRC1%-2	45	3.34	23/0.22	recycled	SFRSCC
[29]	FRC60-1	60	3.26	60/0.75	Steel, HE	SFRC

The casting of the samples from [24,27,29] was performed according to the recommendations of [38]. The fib guidance of [40] was followed by [31]. All notched beam samples were molded with  $600 \times 150 \times 150 \text{ mm}^3$ .

These studies were chosen because they show results of the inverse analysis procedure compatible with the methodology developed in this study for comparison purposes. A similar process of inverse analysis by parts to [27] was used, despite using FEM. Therefore, this feature differs from the one in this study, which used an analytical methodology. Thus, it is possible to investigate the difference between FEM and analytical methodology when comparing their results with those developed here.

An analytical methodology has already been used [30], but the inverse analysis procedure with piecewise process has not been applied. Recycled fibers have been investigated [24], although most studies have used the usual steel fibers. Distinct from the other consulted authors, an SFRC was used [29], and their model was based on [11] and consequently presented some differences in the analytical methodology of [31].

For all these consulted literatures [24,27,29,31], the  $f_{ct}$  parameter is different. The fibers present different values of  $L_f$  and  $d_f$ . The  $f_{ck}$  variation range (45–60 MPa) contemplates a very usual situation when considering conventional SFRC structures. Thus, it is possible to compare the methodology of this study in these different situations and use concretes with typical characteristics.

## 5. Results and Discussions

### 5.1. Generalities

The algorithm studied in this study was used to verify the post-cracking behavior of the concretes presented in Table 1. This study's inverse piecewise analysis methodology achieves the results discussed in this section. The  $(F - CMOD)_{anal}$  curves obtained through the proposed procedure were compared with the results obtained experimentally by the respective references. All the curves obtained analytically through the implemented algorithm were very close to the experimental curves. The errors found were less than 10%.

The illustration of the detailed parameters determination steps for the curves  $(F - CMOD)_{anal}$  will only be shown for the SFRSCC B concrete from [27]. The discussions of this analysis can be found in Section 5.2, Section 5.3, Section 5.4, Section 5.5. The results of the final  $F - CMOD$  diagrams are presented in Section 5.6. The inverse analysis  $(\sigma - w)$  was compared to the consulted authors. Discussions on these results are set out in Section 5.7.

### 5.2. Determination of $f_{ct}$

In this step, the analytical model was processed for the  $f_{ct}/f_{ctm}$  relations presented in Section 4.2.2. Figure 9 shows the results for the secondary parameter  $\sigma_1/f_{ct} = 0.8$  and Figure 10 for  $\sigma_1/f_{ct} = 1.2$ . In Figure 9, secondary parameter has a lower value than the one seen in Figure 10. As a result, there is a trend towards a lower slope for the curves obtained by the algorithm for the different simulated  $f_{ct}/f_{ctm}$  about the dashed curve (experimentally validated by [27]). For better curves visibility obtained through the analytical model, the interval with the CMOD ranges from 0 to  $L_f/175$  was selected to determinate the areas, as indicated in Section 4.2.6, Figures 9 and 10.

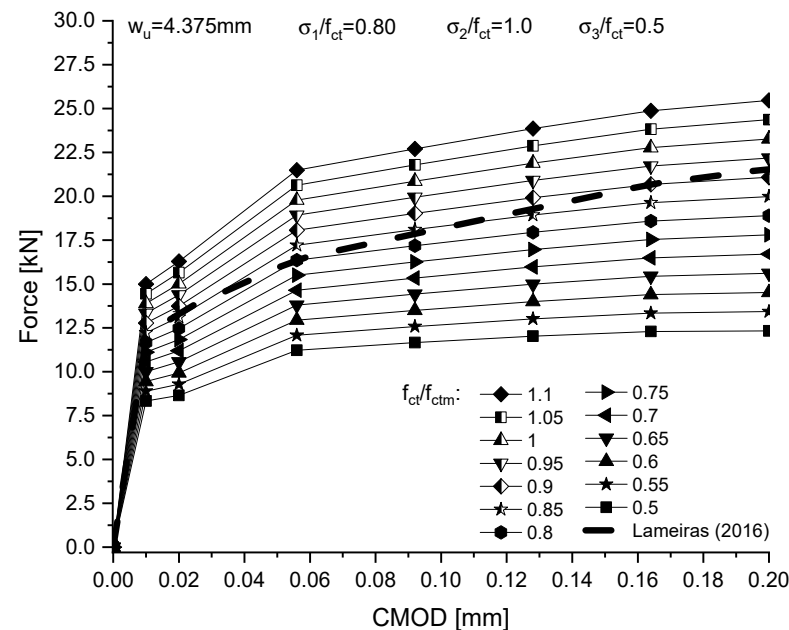


**Figure 9.** Inverse analysis—determination of  $f_{ct}$  for  $\sigma_1/f_{ct} = 0.8$  compared with experimental result of [27].

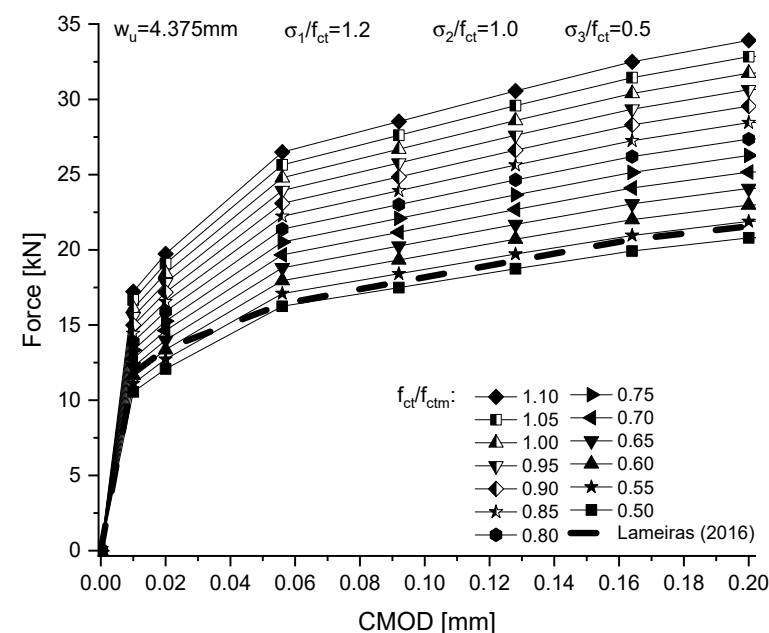


**Figure 10.** Inverse analysis—determination of  $f_{ct}$  for  $\sigma_1/f_{ct} = 1.2$  compared with experimental result of [27].

After executing the step described in Section 4.2.6, the algorithm shows the error found between analytical and experimental curve for the two situations of  $\sigma_1/f_{ct}$ . For the ratio  $\sigma_1/f_{ct} = 0.8$ , among the corresponding  $f_{ct}/f_{ctm}$  parameters, as shown in Figure 9, the smallest error was 5.2%. However, for the ratio  $\sigma_1/f_{ct} = 1.2$  (Figure 10), the smallest error was 2.6%. This result was obtained for the curve corresponding to  $f_{ct}/f_{ctm} = 0.55$ . This curve indicates good compatibility with the dashed curve. The algorithm selected this curve to compose the result in the interval corresponding to this step. There is a significant sensitivity of the results obtained for  $(F - CMOD)_{anal}$  when changing  $f_{ct}/f_{ctm}$ .

### 5.3. Determination of $\sigma_1$

The analytical model was processed for the different  $\sigma_1/f_{ct}$  ratios in this step, according to Section 4.2.3. The results are shown in Figures 11 and 12. For better visibility of the curves obtained through the analytical model, the interval with the CMOD varying from 0 to  $L_f/70$  was selected to estimate the areas, as described in Section 4.2.6. For CMOD between 0 and 0.02 mm, the presented diagram is influenced by the previous step since the  $f_{ct}$  parameter is fixed, and its influences the initial section of the curve. Therefore, this curve is compatible with the experimental response. After  $CMOD = 0.01$  mm, the influence of the  $\sigma_1/f_{ct}$  variation is verified. The observation described in the previous item can be carried out regarding the secondary parameter (which in this step is  $\sigma_2/f_{ct}$ ). However, it is possible to verify less sensitivity of the results obtained concerning the variation of this parameter, which can be seen by comparing Figure 11 with Figure 12 considering the slope of the curve.

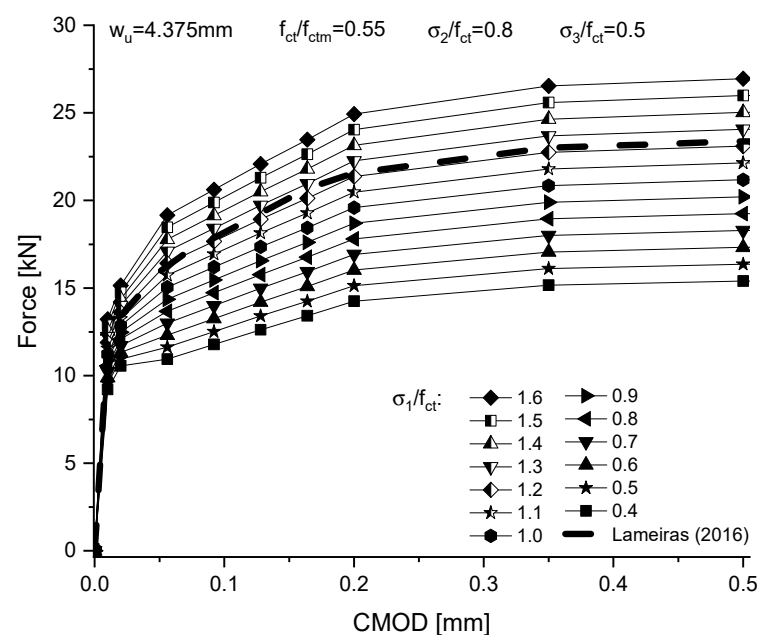


**Figure 11.** Inverse analysis—determination of  $\sigma_1$  for  $\sigma_2/f_{ct} = 0.8$  compared with experimental result of [27].

For the  $\sigma_2/f_{ct} = 0.8$  ratio, among the corresponding  $f_{ct}/f_{ctm}$  parameters, as shown in Figure 11, the smallest error was 1.1% for the  $\sigma_1/f_{ct} = 1.2$  ratio. The algorithm selected this curve to compose the result in the interval corresponding to this step. For the relation  $\sigma_2/f_{ct} = 1.2$  (Figure 12), the slightest error was obtained for the curve corresponding to  $\sigma_1/f_{ct} = 0.8$ . In Figure 11, the curve with this relation is the one that comes closest to the validated result (dashed curve). Based on the association found by the model, the difference between areas of the analytical response to the experimental one was significantly lower, which would not seriously compromise the proposed methodology.



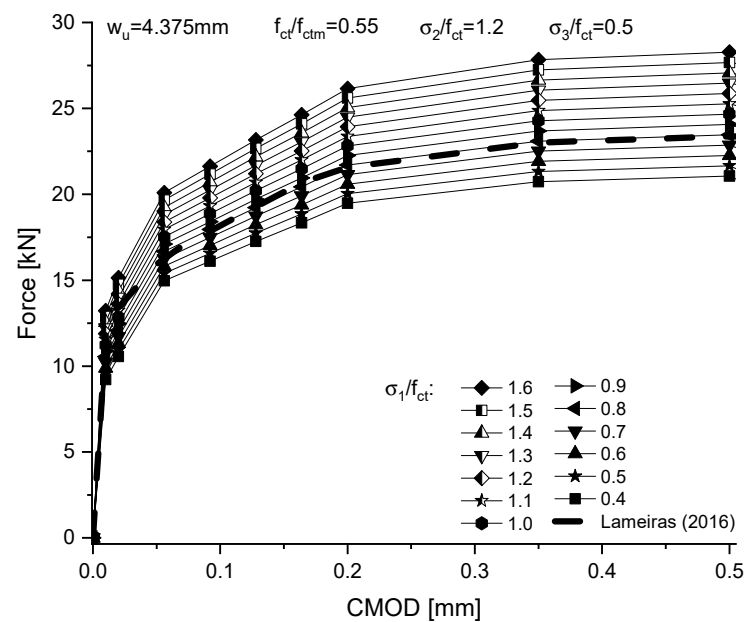


**Figure 12.** Inverse analysis—determination of  $\sigma_1$  for  $\sigma_2/f_{ct} = 1.2$  compared with experimental result of [27].

#### 5.4. Determination of $\sigma_2$

The results of this step are presented in Figure 13 (secondary variable:  $\sigma_3/f_{ct} = 1.2$ ) and in Figure 14 ( $\sigma_3/f_{ct} = 0.8$ ). The interval was selected in these figures with the CMOD varying from 0 to  $L_f/17.5$  and for prediction of areas, as described in Section 4.2.6. A more significant influence of this variable is observed from  $\text{CMOD} = 0.8$ , where the  $\sigma_3/f_{ct} = 1.2$  curve tends to present larger load values, which can be explained by the bigger value of the  $\sigma_3/f_{ct}$  ratio in this situation. The smallest error found in this step is 0.6%, which was obtained for the relation  $\sigma_3/f_{ct} = 0.8$  and  $\sigma_2/f_{ct} = 0.8$ . In the interval between 0 and 0.2 mm, the section of the curve obtained in the previous step is shown. Between 0.2 and 2 mm, the diagram section influenced by the parameters of this step analysis is shown.

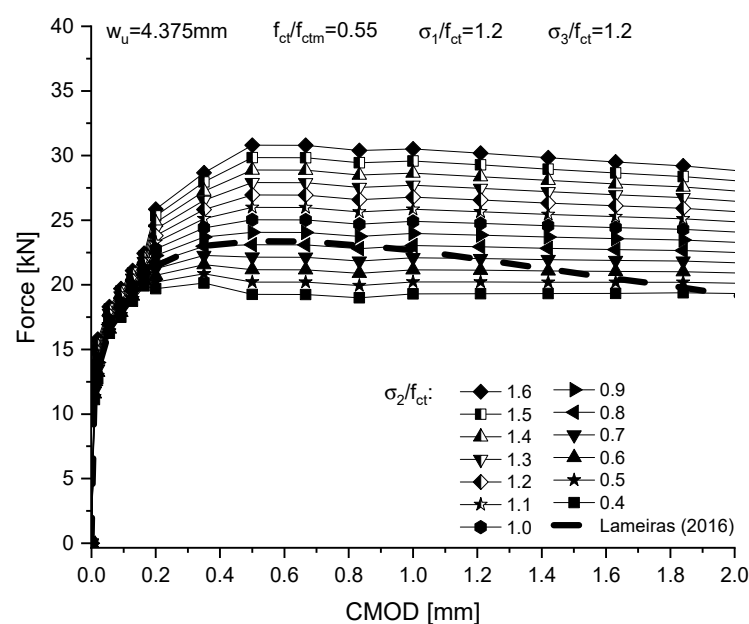


**Figure 13.** Inverse analysis—determination of  $\sigma_2$  for  $\sigma_3/f_{ct} = 1.2$  compared with experimental result of [27].

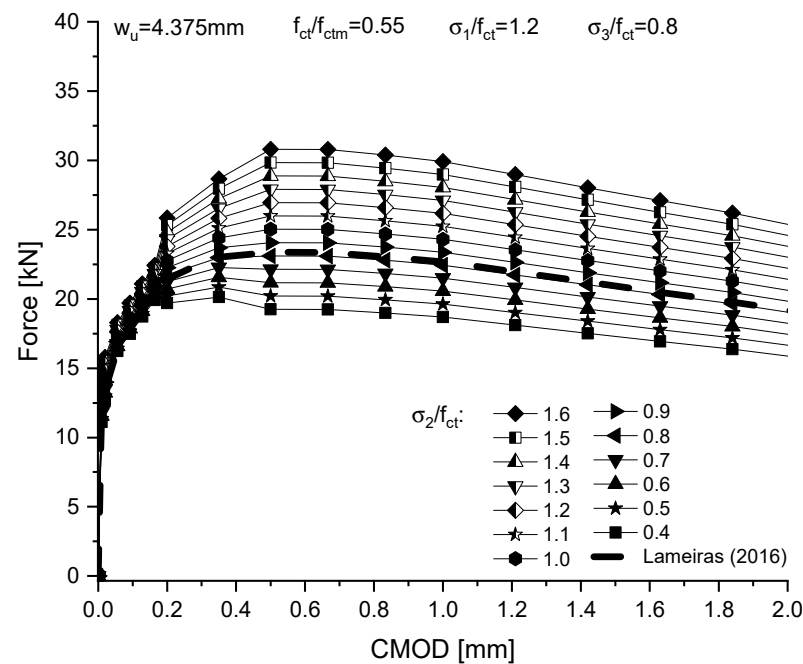


**Figure 14.** Inverse analysis—determination of  $\sigma_2$  for  $\sigma_3/f_{ct} = 0.8$  compared with experimental result of [27].

#### 5.5. Determination of $\sigma_3$

The results of this step are shown in Figures 15–17, which were generated for  $w_u$  corresponding to  $L_f/8$ ,  $L_f/10$ , and  $L_f/4$ , respectively, as described in Section 4.2.6. The visualization interval was selected in these figures with the CMOD varying from 0 to  $L_f/17.5$  and for calculation of areas, as defined in Section 4.2.6. The diagrams showed minor differences between them. The most significant differences occur for  $CMOD > 2.5$ , which is already a high value to evaluate the structural behavior of FRC. The most negligible contrast between the analytical and experimental areas is for  $w_u = 4.375 \text{ mm}$  and  $\sigma_3/f_{ct} = 0.7$ .

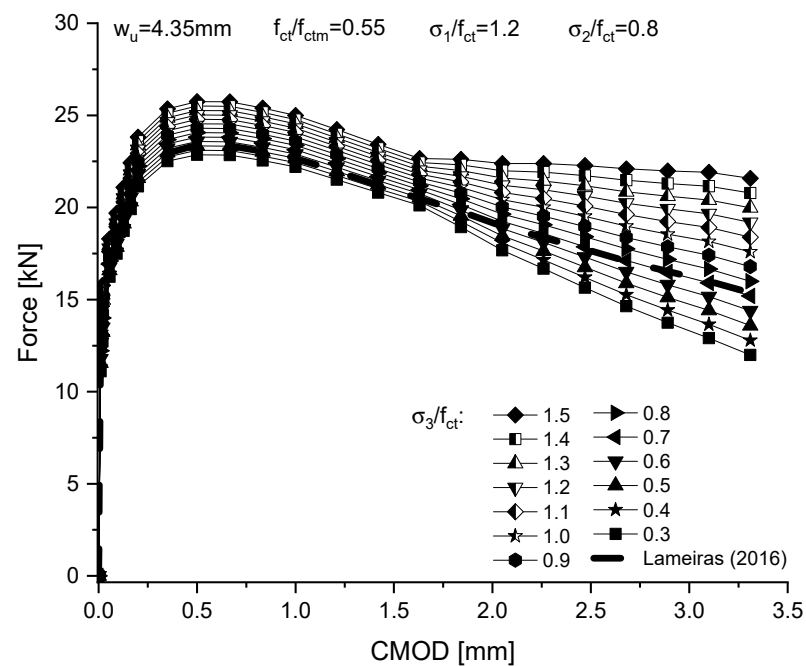


**Figure 15.** Inverse analysis—determination of  $\sigma_3$  for  $w_u = 4.375 \text{ mm}$  compared with experimental result of [27].

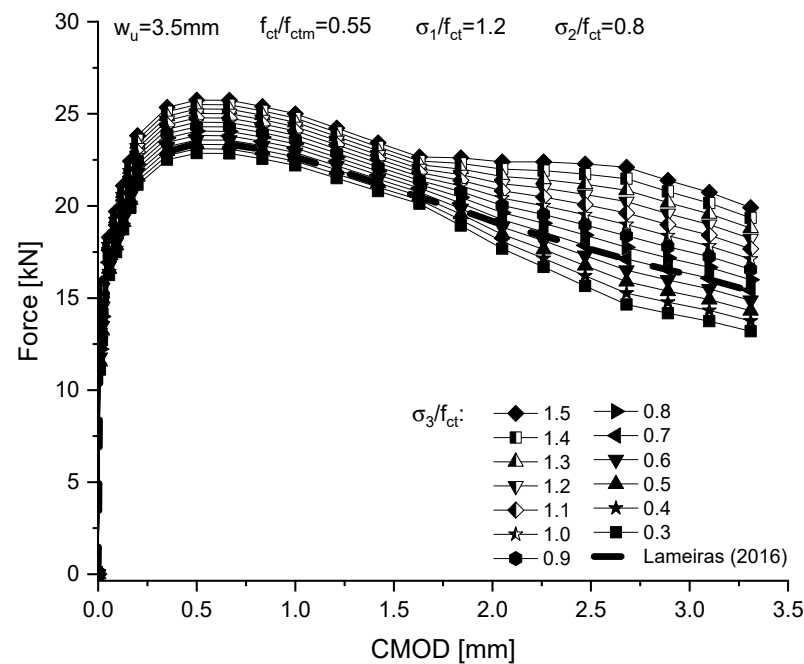


**Figure 16.** Inverse analysis—determination of  $\sigma_3$  for  $w_u = 3.5$  mm compared with experimental result of [27].

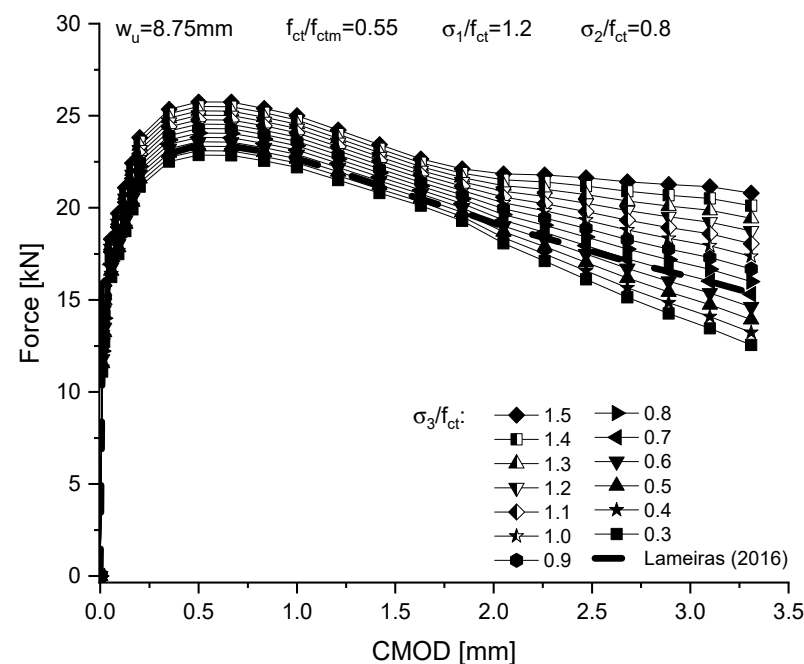


**Figure 17.** Inverse analysis—determination of  $\sigma_3$  for  $w_u = 8.75$  mm compared with experimental result of [27].

From the results presented in Figures 9–17, it is possible to verify that for each situation (determination of  $f_{ct}$ ,  $s_1$ ,  $s_2$ , and  $s_3$ ), a curve approaches the experimental response with a relatively small error (less than 10%). This fact indicates that Equations (9) and (10) well represent the variation of the parameters and that the values of  $q$ ,  $c_1$ , and  $c_2$  were sufficient for the behavior expression.

When the secondary variable changes, i.e., Figure 9 vs. Figure 10, Figure 11 vs. Figure 12, Figure 13 vs. Figure 14, Figure 15 vs. Figure 16, and Figure 17, it is observed that

there is sensitivity for this variable, mainly for  $f_{ct}$ ,  $s_1$ ,  $s_2$ , and  $s_3$ . For the variable  $w_u$ , the sensitivity is lower (Figures 15–17). Lameiras (2016) reached a similar conclusion.

### 5.6. $F - CMOD$ Full Diagram

Figure 18 shows the final  $F - CMOD$  diagram obtained through the analytical model for the inverse analysis and the experimental result presented by [27]. The determined results are close, as shown in the initial sections of the diagrams from Figures 11–17. The same approach of this study was applied to concretes C45-f90, RSFRC1%\_2, and FRC60-1 [24,27,29,31]. The results for these concretes are presented from Figures 18–21.

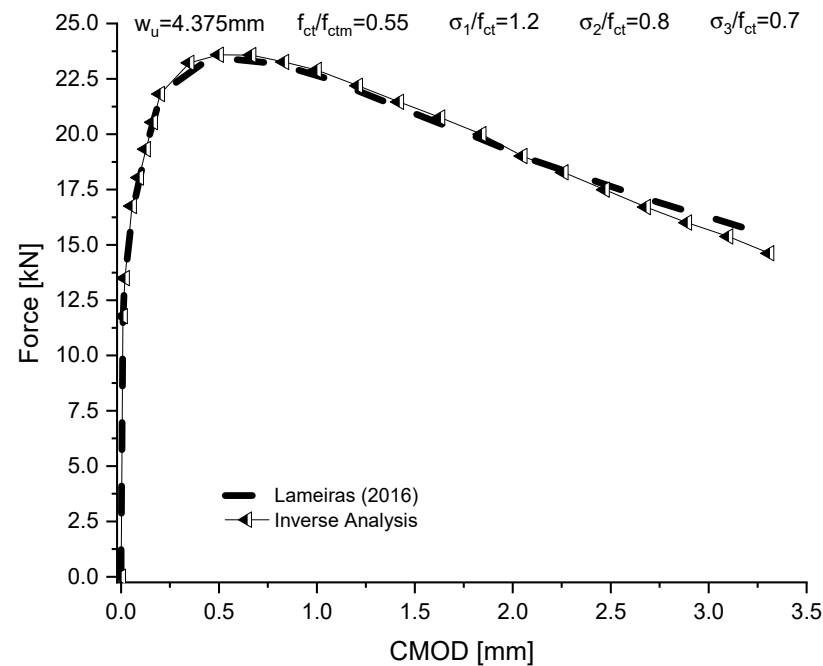


Figure 18. Force–CMOD diagram for SFRSCC B concrete compared with experimental result of [27].

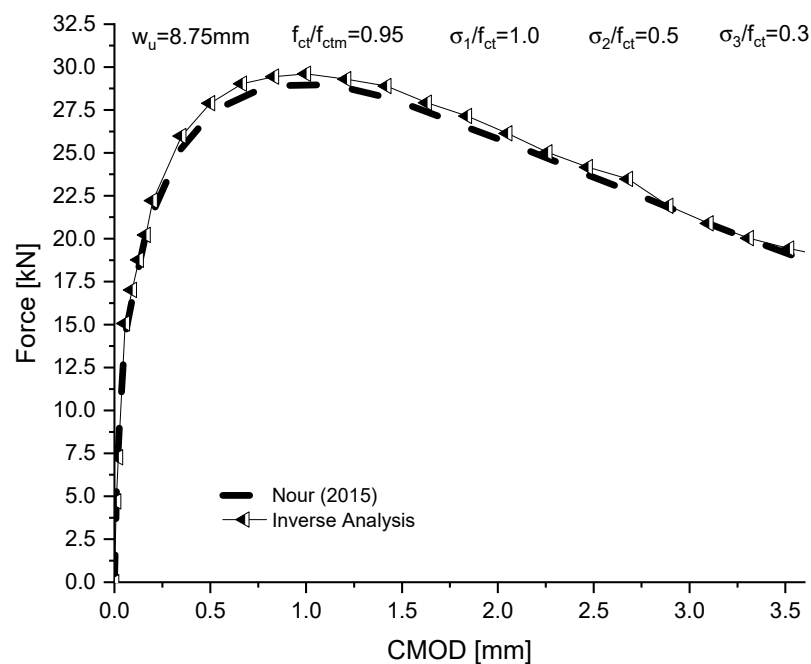


Figure 19. Force–CMOD diagram for FRC60-1 concrete compared with experimental result of [29].

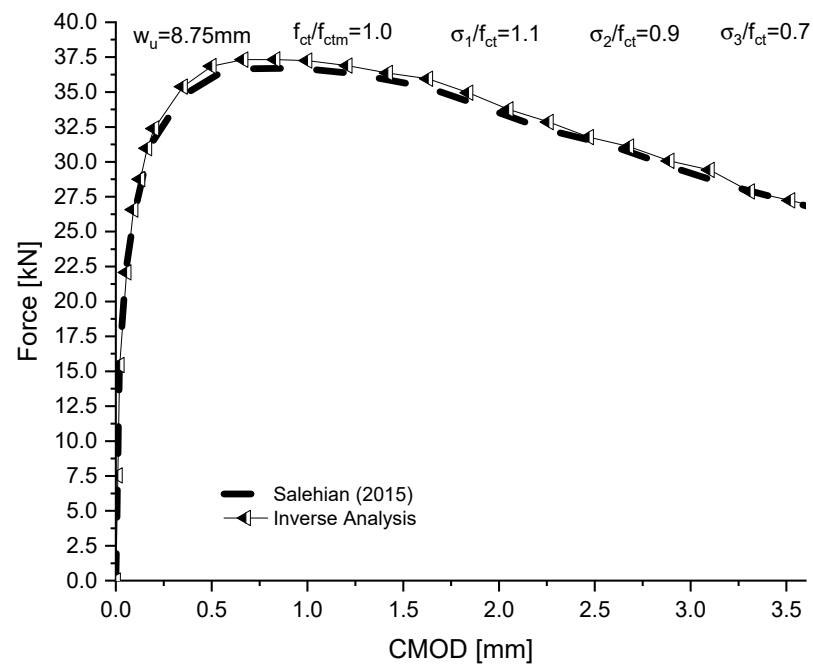


Figure 20. Force–CMOD diagram for C45-f90 concrete compared with experimental result of [31].

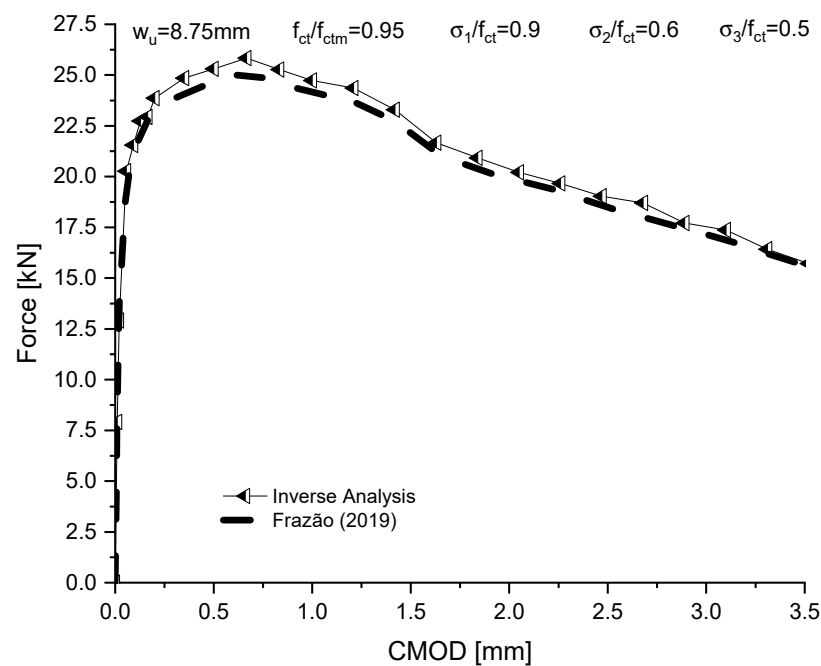
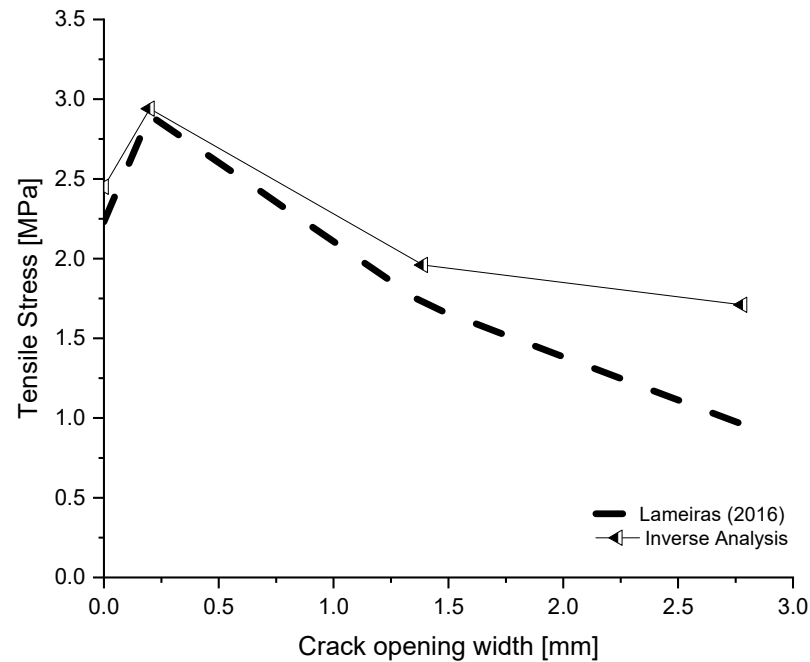


Figure 21. Force–CMOD diagram for RSFRC1%\_2 concrete compared with experimental result of [24].

The analytical model used to obtain the  $F - CMOD$  curves proved to be quite adequate, even with varying characteristics of concrete and fibers. Satisfactory results were noticed even for RSFRC1%\_2, which has a different type of fiber (steel fiber recycled from tires). In determining the compression behavior, the model of [31], which this study used to generate the  $F - CMOD$  curves, employs the model described in [42] later modified by [43] to represent  $\sigma_{cc} - \varepsilon_{cc}$ . This model includes equations formulated for hooked steel fibers. Although these equations were not calibrated for a different type of fiber; however, the results were satisfactory. This evidence is explained because the compressive behavior of the composite has less influence on the post-cracking behavior.

### 5.7. Inverse Analysis

As a final result of the inverse analysis using the approach of this study, the  $\sigma - w$  diagrams are presented in Figures 22–25. The values of  $\sigma_1, \sigma_2, \sigma_3, w_1, w_2, w_3$ , and  $w_u$  are shown in Table 2. For these parameters, the consulted authors used different values from the literature. For comparison purposes, these parameters were graphically collected from these references, and the values found through the determined approach are presented.



**Figure 22.** Stress–COD diagram obtained through inverse analysis for concrete SFRSCC B compared with experimental result of [27].

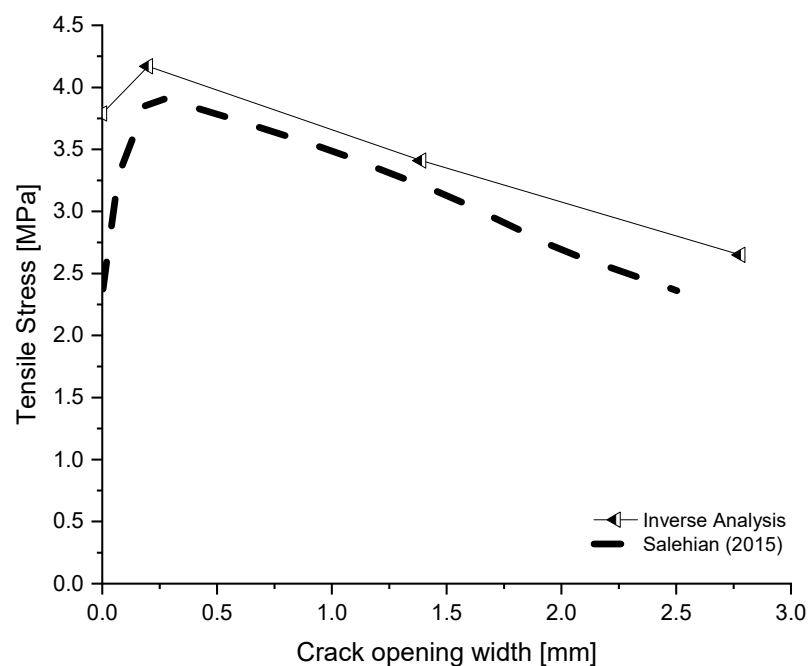


**Figure 23.** Stress–COD diagram obtained through inverse analysis for concrete C45-f90 compared with experimental result of [31].

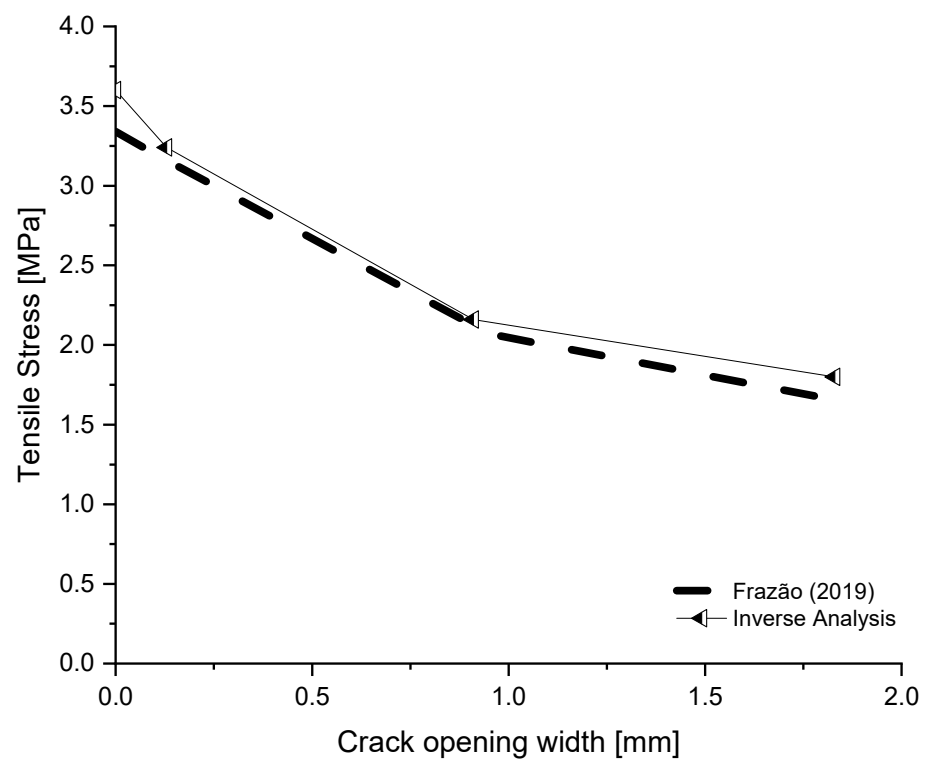


**Figure 24.** Stress–COD diagram obtained through inverse analysis for concrete RSFRC1%\_2 compared with experimental result of [24].

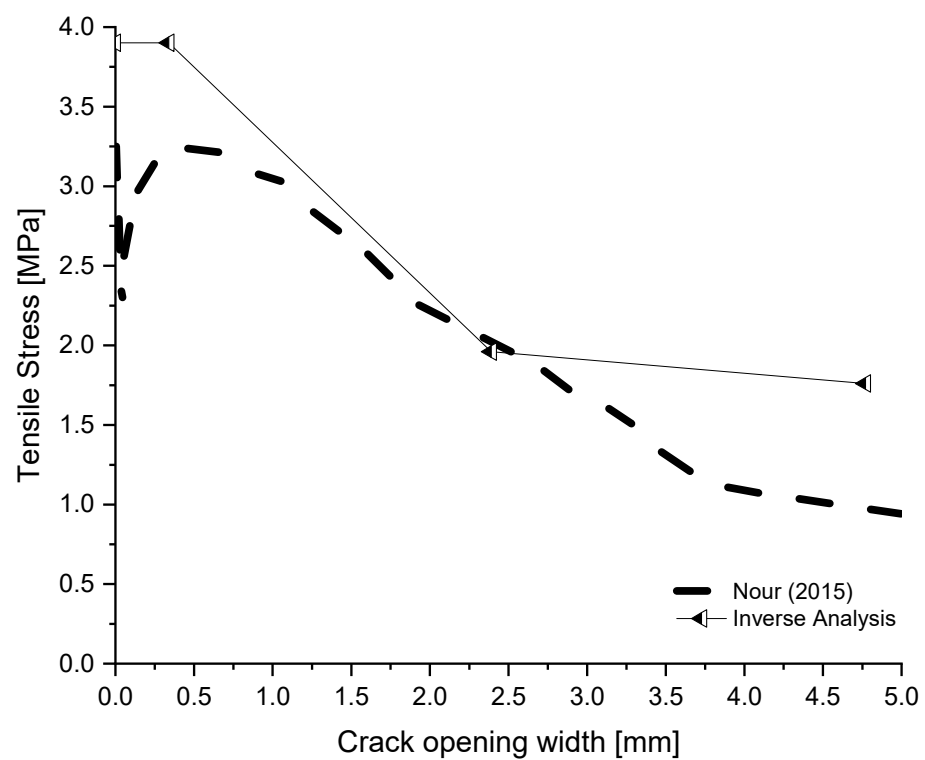


**Figure 25.** Stress–COD diagram obtained through inverse analysis for concrete FRC60-1 compared with experimental result of [29].



**Table 2.** Parameters from the inverse analysis for different FRC types.

Concrete	Reference	$f_{ct}$ [MPa]	$w_1$ [mm]	$\sigma_1$ [-]	$w_2$ [mm]	$\sigma_2$ [-]	$w_3$ [mm]	$\sigma_3$ [-]	$w_u$ [mm]
SFRSCC B	This study	2.45	0.20	2.94	1.39	1.96	2.78	1.71	4.38
	[27]	2.23	0.20	2.90	1.40	1.71	2.80	0.95	4.38
C45-f90	This study	3.79	0.20	4.17	1.39	3.41	2.78	2.65	8.75
	[31]	3.60	0.20	3.92	1.50	3.25	2.50	2.36	2.50
RSFRC1%-2	This study	3.60	0.13	3.24	0.91	2.16	1.83	1.80	8.75
	[24]	3.34	0.10	3.20	0.95	2.07	1.80	1.67	2.50
FRC60-1	This study	3.30	0.34	3.30	2.39	1.65	4.77	0.99	8.75
	[29]	3.26	0.30	3.16	2.40	1.49	4.80	0.82	2.50

The  $f_{ctm}$  was calculated according to [40] for concrete C45-f90 [31] and according to [50] for concrete SFRSCC B [27]. This resulted in slightly different values for this parameter. However, this did not significantly affect the results up to  $COD = 1.4$  mm since the value of  $f_{ct}$  determined in this study was also higher.

Some differences between the studies in the literature and the results were found here, explained by the studies using different FRC behavior models. First, the values used for  $w_1$ ,  $w_2$ , and  $w_3$  in the literature were different from those applied based on the methodology employed here. When this difference was significant, some interpolations were performed to compare with closer  $w$  values (Table 2). Sensitivity can be observed in the variation of parameters  $w_1$ ,  $w_2$ , and  $w_3$ .

Figures 22–25 show the Tensile vs. Crack width for the considered concretes compared to the literature results. Generally, it is possible to observe a reasonable agreement between the results. In addition, the FRC behavior model used in this study is validated by the literature. In turn, the acceptable feasibility of using the methodology of this study can be stated.

Compared with different inverse analysis procedures, the process carried out has the advantage of establishing consistent criteria as a function of fiber length to then determine the parameters  $w_1$ ,  $w_2$ , and  $w_3$ . Furthermore, the progressive method of determining the inverse analysis parameters leads to quick and efficient processing of the developed algorithm.

## 6. Conclusions

This study proposes a methodology for performing the inverse analysis procedure. A computational algorithm is developed based on a well-validated analytical model for the behavior of FRC. Criteria for determining parameters are adopted as a function of fiber length, which is an essential factor for the tensile behavior of this type of concrete.

A progressive procedure for parameter estimation is proposed. The methodology proved to be quick (the analyses were performed in less than two minutes) and effective in determining stress vs. COD. The procedure is adequately validated by comparing the results obtained with different literature and for different types of concrete and fibers with various characteristics. The results indicated a sensitivity of the developed algorithm to the inverse analysis parameters.

The curves obtained are similar to the experimental responses in the literature, even with the relatively simple methodology to perform the inverse analysis procedure employed in determining  $F - CMOD$  and  $\sigma - w$ .

With the development of this study, it is possible to conclude that:

- The inverse analysis can be performed with the procedure proposed, obtaining results compatible with the experimental response, considering a margin of error of less than 10%;

- The methodology developed reduces the number of iterations of the developed algorithm, providing faster processing;
- This procedure does not require FEM software.

As a proposal for future studies, applying the procedure used in this study for larger structures and applying this methodology in other types of bending tests are recommended. In addition, the authors recommend future validation of this methodology in another study, also using finite element software. Finally, another study may be to conduct a reliability analysis to evaluate the method's reliability.

**Author Contributions:** Conceptualization, P.P.M.d.C. and R.d.M.L.; methodology, P.P.M.d.C. and R.d.M.L.; software, P.P.M.d.C.; validation, P.P.M.d.C.; writing—original draft preparation, P.P.M.d.C. and R.d.M.L.; writing—review and editing, P.P.M.d.C. and R.d.M.L.; supervision, R.d.M.L.; project administration, R.d.M.L. All authors have read and agreed to the published version of the manuscript. All authors have contributed substantially to the study reported.

**Funding:** This research received no external funding.

**Data Availability Statement:** The data reported in this article are available from the corresponding author upon request.

**Acknowledgments:** The authors would like to thank the University of Brasilia and Federal University of Western Bahia for the support provided to carry out this research.

**Conflicts of Interest:** The authors declare no conflict of interest.

## References

1. Ledesma Villalba, A. Identificación de Parámetros en Geotecnia: Aplicación a la Excavación de Túneles. Ph.D. Thesis, Universitat Politècnica de Catalunya, Barcelona, Spain, 1987.
2. Almeida, L.C.D. Identificação de Parâmetros Estruturais com Emprego de Análise Inversa. Ph.D. Thesis, Universidade Estadual de Campinas, Campinas, Brazil, 2006. [\[CrossRef\]](#)
3. Rauecker, J.C.N.; Pereira Junior, W.M.; Pituba, J.J.C.; Araújo, D.L. Uma abordagem experimental e numérica para determinação de curvas de compressão para concreto simples e reforçados com fibras de aço. *Rev. Mater.* **2019**, *24*. [\[CrossRef\]](#)
4. Oliveira, F.L. Design-Oriented Constitutive Model for Steel Fiber Reinforced Concrete. Ph.D. Thesis, Universitat Politècnica de Catalunya, Barcelona, Spain, 2010.
5. Mobasher, B.; Bakhshi, M.; Barsby, C. Backcalculation of residual tensile strength of regular and high performance fiber reinforced concrete from flexural tests. *Construct. Build. Mater.* **2014**, *70*, 243–253. [\[CrossRef\]](#)
6. Di Prisco, M.; Plizzari, G.; Vandewalle, L. Fibre reinforced concrete: New design perspectives. *Mater. Struct.* **2009**, *42*, 1261–1281. [\[CrossRef\]](#)
7. ACI Committee 544. State-of-the-art report on fiber reinforced concrete. *ACI Struct. J.* **1997**, *70*, 729–744. [\[CrossRef\]](#)
8. AASHTO-AGC-ARTBA. *The Use of State-of-the-Practice of Fiber Reinforced Concrete*; Subcommittee on New Highway Materials. Task Force 36 Report; AASHTO-Associated General Contractors of America-American Road and Transportation Builders Association Joint Committee: Washington, DC, USA, 2001.
9. Singh, H. *Steel Fiber Reinforced Concrete: Behavior, Modelling and Design*; Springer: Ludhiana, India, 2016.
10. Hillerborg, A. Analysis of fracture by means of the fictitious crack model, particularly for fiber reinforced concrete. *Int. J. Cem. Compos.* **1980**, *2*, 177–184.
11. Zhang, J.; Stang, H. Applications of stress crack width relationship in predicting the flexural behavior of fibre-reinforced concrete. *Cem. Concr. Res.* **1998**, *28*, 439–452. [\[CrossRef\]](#)
12. Accornero, F.; Rubino, A.; Carpinteri, A. Post-cracking regimes in the flexural behaviour of fibre-reinforced concrete beams. *Int. J. Solids Struct.* **2022**, *248*, 111637. [\[CrossRef\]](#)
13. Fantilli, A.P.; Chiaia, B.; Gorino, A. Unified approach for minimum reinforcement of concrete beams. *ACI Struct. J.* **2016**, *5*, 1107–1116. [\[CrossRef\]](#)
14. Fantilli, A.P.; Chiaia, B.; Gorino, A. Fiber volume fraction and ductility Index of concrete beams. *Cem. Concr. Compos.* **2016**, *65*, 139–149. [\[CrossRef\]](#)
15. Gorino, A.; Fantilli, A.P. Scaled Approach to Designing the Minimum Hybrid Reinforcement of Concrete Beams. *Materials* **2020**, *13*, 5166. [\[CrossRef\]](#)
16. Naaman, A.E.; Reinhardt, H.W. Proposed classification of HPFRC composites based on their tensile response. *Mater. Struct.* **2006**, *5*, 547–555. [\[CrossRef\]](#)
17. Cunha, V.M.D.C.F. Steel Fibre Reinforced Self-Compacting Concrete (from Micro-Mechanics to Composite Behaviour). Ph.D. Thesis, Universidade do Minho, Braga, Portugal, 2010.

18. Azevedo, A.F.M.; Barros, J.A.O.; Sena-Cruz, J.M.; Gouveia, A.V. Software in structural engineering education and design. In Proceedings of the III Portuguese-Mozambican Conference of Engineering, Maputo, Mozambique, 19–21 August 2003.
19. Abrishambaf, A.; Barros, J.A.O.; Cunha, V.M.C.F. Tensile stress–crack width law for steel fibre reinforced self-compacting concrete obtained from indirect (splitting) tensile tests. *Cem. Concr. Compos.* **2015**, *57*, 153–165. [\[CrossRef\]](#)
20. Roelfstra, P.E.; Wittmann, F.H. Numerical method to link strain softening with failure of concrete. In *Fracture Toughness and Fracture Energy of Concrete*; Elsevier: Amsterdam, The Netherlands, 1986.
21. Löfgren, I.; Stang, H.; Olesen, J.F. Fracture Properties of FRC Determined through Inverse Analysis of Wedge Splitting and Three-Point Bending Tests. *J. Adv. Concr. Technol.* **2005**, *3*, 423–434. [\[CrossRef\]](#)
22. Gao, D.; Ding, C.; Yuyang, P.; Chen, G. An inverse analysis method for multi-linear tensile stress-crack opening relationship of 3D/4D/5D steel fiber reinforced concrete. *Construct. Build. Mater.* **2021**, *309*, 125074. [\[CrossRef\]](#)
23. Zhang, J.; Li, V.C. Simulation of crack propagation in fiber-reinforced concrete by fracture mechanics. *Cem. Concr. Res.* **2004**, *34*, 333–339. [\[CrossRef\]](#)
24. Frazão, C.M.V. Recycled Steel Fiber Reinforced Concrete for Structural Elements Subjected to Chloride Attack: Mechanical and Durability Performance. Ph.D. Thesis, Universidade do Minho, Braga, Portugal, 2019.
25. Blasi, G.; Leone, M. Inverse analysis-based model for the tensile behaviour of fibre-reinforced concrete with manufactured and waste tyres recovered fibres. *Case Stud.* **2022**, *17*, e01297. [\[CrossRef\]](#)
26. Santos, F.L.G.D.; Forti, T.L.D. Concrete cohesive curves for specimens with different sizes: A study of inverse analysis and size effect. *Eng. Fract. Mech.* **2022**, *261*, 108249. [\[CrossRef\]](#)
27. Lameiras, R.D.M. Sandwich Structural Panels Comprising Thin-Walled SFRSCC and GFRP Connectors: From Material Features to Structural Behaviour. Ph.D. Thesis, Universidade do Minho, Braga, Portugal, 2016.
28. Nour, A.; Massicotte, B.; Montaignac, R.; Charron, J.-P. Derivation of a crack opening deflection relationship for fibre reinforced concrete panels using a stochastic model: Application for predicting the flexural behaviour of round panels using stress crack opening diagrams. *Cem. Concr. Res.* **2011**, *41*, 964–974. [\[CrossRef\]](#)
29. Nour, A.; Massicotte, B.; Montaignac, R.; Charron, J.-P. Development of an inverse analysis procedure for the characterisation of softening diagrams for FRC beams and panels. *Construct. Build. Mater.* **2015**, *94*, 35–44. [\[CrossRef\]](#)
30. Olesen, J.F. Fictitious Crack Propagation in Fiber-Reinforced Concrete Beams. *J. Eng. Mech.* **2001**, *127*, 272–280. [\[CrossRef\]](#)
31. Salehian, H. Evaluation of the Performance of Steel Fibre Reinforced Self-Compacting Concrete in Elevated Slab Systems; From the Material to the Structure. Ph.D. Thesis, Universidade do Minho, Braga, Portugal, 2015.
32. Stephen, S.J.; Raphael, B.; Gettu, R.; Jose, S. Determination of the tensile constitutive relations of fiber reinforced concrete using inverse analysis. *Construct. Build. Mater.* **2019**, *195*, 405–414. [\[CrossRef\]](#)
33. Ding, C.; Gao, D.; Guo, A. Analytical methods for stress-crack width relationship and residual flexural strengths of 3D/4D/5D steel fiber reinforced concrete. *Construct. Build. Mater.* **2022**, *346*, 128438. [\[CrossRef\]](#)
34. Zhang, J.; Ju, X. Investigation on stress-crack opening relationship of engineered cementitious composites using inverse approach. *Cem. Concr. Res.* **2011**, *41*, 903–912. [\[CrossRef\]](#)
35. Matos, L.M.P.; Barros, J.A.O.; Ventura-Gouveia, A.; Calçada, R.A.B. A new inverse analysis approach for predicting the fracture mode I parameters of fibre reinforced concrete. *Eng. Fract. Mech.* **2021**, *246*, 107613. [\[CrossRef\]](#)
36. Meng, G.; Wu, B.; Xu, S.; Huang, J. Modelling and experimental validation of flexural tensile properties of steel fiber reinforced concrete. *Construct. Build. Mater.* **2021**, *273*, 121974. [\[CrossRef\]](#)
37. Metha, P.K.; Monteiro, P.J.M. *Concrete, Microestrutura, Propriedades e Materiais*, 3rd ed.; IBRACON: São Paulo, Brazil, 2008.
38. EN 14651; Test Method for Metallic Fibered Concrete—Measuring the Flexural Tensile Strength (Limit of Proportionality (LOP), residual). European Committee for Standardization: Brussels, Belgium, 2005.
39. RILEM. Technical Committee TDF-162. Test and design methods for steel fibre reinforced concrete—Design of steel fibre reinforced concrete using the  $\sigma$ -w method: Principles and application. *J. Mater. Struct.* **2002**, *35*, 262–276.
40. FIB. *Model Code 2010*; International Federation for Structural Concrete: Lausanne, Switzerland, 2010.
41. Van Mier, J.G.M.; Mechtcherine, V. Minimum demands for deformation-controlled uniaxial tensile tests. In *Final Report of TC 187-SOC 39: Experimental Determination of the Stress-Crack Opening Curve for Concrete in Tension*; Planas, J.M., Ed.; RILEM Technical Committee: Bagneux, France, 2007; pp. 5–11.
42. Vipulanandan, C.; Paul, E. Performance of epoxy and polyester polymer concrete. *ACI Mater. J.* **1990**, *87*, 241–251. [\[CrossRef\]](#)
43. Barros, J.A.; Figueiras, J.A. Flexural behavior of SFRC: Testing and modeling. *J. Mater. Civ. Eng.* **1999**, *11*, 331–339. [\[CrossRef\]](#)
44. Hillerborg, A.; Modéer, M.; Petersson, P.E. Analysis of crack formation and crack growth in concrete by means of fracture mechanics and finite elements. *Cem. Concr. Res.* **1976**, *6*, 773–781. [\[CrossRef\]](#)
45. Massicotte, B. Implementing SFRC design into North American codes: Application to a building floor. In Proceedings of the Invited paper to the International Workshop on the Advanced in Fibre Reinforced Concrete, Bergamo, Italy, 24–25 September 2004.
46. Ulfkjaer, J.; Krenk, S.; Brincker, R. Analytical model for fictitious crack propagation in concrete beams. *J. Eng. Mech.* **1995**, *121*, 7–15. [\[CrossRef\]](#)
47. Kooiman, A.G. Modelling Steel Fibre Reinforced Concrete for Structural Design. Ph.D. Thesis, Technische Universiteit Delft, Delft, The Netherlands, 2000.

48. Iyengar, K.T.S.R.; Raviraj, S.; Ravikumar, P.N. Analysis study of fictitious crack propagation in concrete beams using a bi-linear  $\sigma$ – $w$  relation. In Proceedings of the 3th International Conference on Fracture Mechanics of Concrete and Structure (FRAMCOS III), Gifu, Japan, 12–16 October 1998.
49. Pedersen, C. New Production Processes, Materials and Calculation Techniques for Fiber Reinforced Concrete Pipes. Ph.D. Thesis, Technical University of Denmark, Lyngby, Denmark, 1996.
50. EN 1992-1; European Standard Eurocode 2: Design of Concrete Structures—Part 1: General Rules and Rules for Buildings. EUROCODE 4 EN. CEN—European Committee for Standardisation: Brussels, Belgium, 2004.

**Disclaimer/Publisher’s Note:** The statements, opinions and data contained in all publications are solely those of the individual author(s) and contributor(s) and not of MDPI and/or the editor(s). MDPI and/or the editor(s) disclaim responsibility for any injury to people or property resulting from any ideas, methods, instructions or products referred to in the content.